

2007

Magnetization Dynamics and Anisotropy in Ferromagnetic/ Antiferromagnetic Ni/NiO Bilayers

andreas Petersen

College of William & Mary - Arts & Sciences

Follow this and additional works at: <https://scholarworks.wm.edu/etd>



Part of the [Condensed Matter Physics Commons](#)

Recommended Citation

Petersen, andreas, "Magnetization Dynamics and Anisotropy in Ferromagnetic/Antiferromagnetic Ni/NiO Bilayers" (2007). *Dissertations, Theses, and Masters Projects*. Paper 1539626855.

<https://dx.doi.org/doi:10.21220/s2-pt5b-9005>

This Thesis is brought to you for free and open access by the Theses, Dissertations, & Master Projects at W&M ScholarWorks. It has been accepted for inclusion in Dissertations, Theses, and Masters Projects by an authorized administrator of W&M ScholarWorks. For more information, please contact scholarworks@wm.edu.

Magnetization Dynamics and Anisotropy in Ferromagnetic/Antiferromagnetic
Ni/NiO Bilayers

Andreas Petersen

Lüneburg, Lower Saxony, Germany

A Thesis presented to the Graduate Faculty
of the College of William and Mary in Candidacy for the Degree of
Master of Science

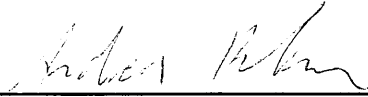
Applied Science

The College of William and Mary
August, 2007

APPROVAL PAGE

This Thesis is submitted in partial fulfillment of the requirements for the
degree of

Master of Science



Andreas Petersen

Approved by the Committee, July, 2007

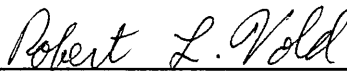


Committee Chair

Associate Professor, Gunter Lüpke, Department of Applied Science
The College of William and Mary



Assistant Professor, Irina Novikova, Department of Physics
The College of William and Mary



Professor, Robert L. Vold, Department of Applied Science
The College of William and Mary

ABSTRACT PAGE

Magnetization dynamics and anisotropy of a Ni/NiO bilayer have been studied by static magneto optical Kerr effect (MOKE) and time resolved pump-probe MOKE. The time domain measurements show coherent magnetization oscillations on the picosecond scale whose frequency fits well to FMR equations used for frequency domain measurements. Anisotropy constants extracted from the time domain data agree with the findings of the static MOKE measurements and reveal tetragonal and uniaxial components induced by the strain in the lattice-mismatched Ni/NiO bilayer. Studies of the Gilbert damping show a strong effect of the sample's anisotropy on the frequency dependence of the damping that has not been mentioned in the literature so far.

Acknowledgements

Completing a master thesis in one year is a hard task and I am glad to have the opportunity to thank those who made this work possible. First and foremost, I would like to thank my advisor, Professor Gunter Lüpke, for his support and guidance throughout the whole process as well as for his review of this work.

Special thanks go to Kevin Smith. He contributed a great deal to this work. His experience made the experiment run, he took data while I was busy with classes and when the theory seemed to make no sense he always had time for a discussion. Without him this work would not have been possible.

I also would like to thank Dr. Haibin Zhao, whom I exposed to a constant stream of questions, especially during the last two months and who always had a useful suggestion, when I was stuck.

I would like to express my appreciation to my thesis committee members, Dr. Irina Novikova and Dr. Robert Vold, for taking the time to be on my thesis committee.

Thanks also to Erik Spahr for proof reading my thesis and to all the other group members for the nice working atmosphere.

Table of Contents

1	Introduction	2
2	Theory	4
2.1	Magneto Optical Kerr Effect – MOKE.....	4
2.2	Demagnetizing Fields.....	7
2.3	Magnetocrystalline Anisotropy.....	9
2.4	Magnetization Dynamics.....	11
2.5	Ferromagnetic Resonance Frequency.....	15
3	Experimental Setup	18
3.1	S-MOKE.....	18
3.2	TR-MOKE.....	19
3.3	Sample.....	21
3.4	Anisotropy Energy.....	23
4	Static MOKE	25
4.1	Measurements.....	25
4.2	Results and Discussion.....	28
5	Time Resolved-MOKE	33
5.1	Measurements.....	33
5.2	Results and Discussion.....	35
6	Damping	46
7	Conclusions	54
8	References	55

List of Figures

- 2.1 Schematic of the Kerr effect. The incoming linearly polarized light can be decomposed into LCP and RCP components which have different amplitudes and phases after reflection from a magnetic medium. This leads to an ellipticity and a rotation of the polarization.5
- 2.2 Sketch of the three main MOKE geometries. They are determined by the orientation of the magnetization with respect to the surface of the sample and to the plane of incidence. The light can be either polarized perpendicular (s) or parallel (p) to the plane of incidence.6
- 2.3 The cross-polarization factor for longitudinal MOKE as a function of the angle of incidence. The highest Kerr response can be achieved at an incidence angle of roughly 65°7
- 2.4 (a) shows a bar magnet in an external field H_{ext} . This field causes the poles and their field lines shown in (b). Those field lines are pointing in the opposite direction of the external field and causing the demagnetization of the sample. The effect decreases with increasing distance between the two poles. (c) shows the effective B field with its closed field lines. Inside the magnet, it still points in the direction of the former external field H_{ext} because the demagnetization field can never exceed the magnetization in magnitude.8
- 2.5 (a) shows a general ellipsoid with its axes a, b and c. If the axes b and c have the same length as in (b) it is called oblate spheroid. This can be considered a thin film in the limit $c \rightarrow \infty$9
- 2.6 Polar plot of the cubic anisotropy energy density (Eq. 7). The left plot represents the case $K_1 > 0$. Here the easy axes are along the cube edges as in the case of iron. The right plot shows the case for $K_1 < 0$. In such a material, like nickel, the easy axes are along the cube diagonals.11
- 2.7 The undamped magnetization vector precesses around the effective magnetic field. ϕ and θ are the aximuthal and polar angles of \vec{M} respectively.12
- 2.8 The magnetization vector precesses according to equation 15. $-\vec{M} \times \vec{H}$ is always perpendicular to \vec{M} and \vec{H} . It causes the precession around \vec{H} whereas $-\vec{M} \times (\vec{M} \times \vec{H})$ causes the damping by pulling the magnetization in the direction of \vec{H}14

2.9	Plots of equation 16 for different values of α .	15
3.1	Schematic of the static MOKE setup. A polarizer analyzer combination is used to measure the polarization rotation due to the magnetization in the sample.	19
3.2	Schematic of the TR-MOKE experimental setup. The path length of the pump beam can be altered via a delay stage, causing the pump beam to arrive at the sample some time Δt before the probe beam. The magnetization oscillations excited by the pump beam are measured with the polarizer analyzer setup. The MOKE signal is recorded as a function of Δt .	20
3.3	Cross sectional TEM image of the sample after in situ annealing. The dark area between Ni and MgO is a 7-8 nm thick NiO layer. It forms during growth of the sample and becomes thicker during further annealing. The bottom left scale corresponds to two nanometers.	22
3.4	Azimuthal dependence of the coercivity for the as grown sample (a) and after in situ annealing (b). The as grown sample exhibits the expected cubic four fold symmetry. The annealing process induces an additional uniaxial anisotropy. The vertical axis corresponds to the coercive field in Oe.	23
4.1	Hysteresis loop measured for $\beta = 180^\circ$. H_{C1} , H_{C2} and H_{EB} are indicated by dashed vertical lines.	26
4.2	Hysteresis loop measured for $\beta = 85^\circ$.	27
4.3	Hysteresis loop measured for $\beta = 55^\circ$. 1, 2 and 3 mark the regions of fast switching, slow switching and saturation of the magnetization, respectively.	27
4.4	Hysteresis loop measured for $\beta = 135^\circ$.	28
4.5	Polar plot of the coercivity field H_c as a function of the external field angle β . Also indicated are selected crystallographic directions and the four directions corresponding to the hysteresis loops shown in figure 4.6.	29
4.6	Hysteresis loops for the four characteristic directions marked in figure 4.5.	29
4.7	Magnetization curves of different crystallographic directions for single crystal nickel. For comparison, the boundaries of region 1, 2 and 3 have the same field value as the regions in figure 4.3.	30
4.8	Magnetization curves of easy and hard direction for single crystal cobalt.	32

5.1	A typical magnetization oscillation measured with TR-MOKE. The external field of 685Oe is oriented along the hard axis ($\beta = 120^\circ$). The timescale on the horizontal axis denotes the time difference between pump and probe beam. For negative times, the probe beam arrives before the pump beam and at $t = 0$, both beams arrive simultaneously.	35
5.2	Magnetization oscillations measured with TR-MOKE. The external field of 51Oe is oriented along the hard axis ($\beta = 120^\circ$). The timescale on the horizontal axis denotes the time difference between pump and probe beam. The red curve is a fit using equation 17.	36
5.3	Magnetization oscillations measured with TR-MOKE. The external field of 232Oe is oriented along the hard axis ($\beta = 120^\circ$). The timescale on the horizontal axis denotes the time difference between pump and probe beam. The red curve is a fit using equation 17.	36
5.4	Magnetization oscillations measured with TR-MOKE. The external field of 459Oe is oriented along the hard axis ($\beta = 120^\circ$). The timescale on the horizontal axis denotes the time difference between pump and probe beam. The red curve is a fit using equation 17.	37
5.5	Magnetization oscillations measured with TR-MOKE. The external field of 685Oe is oriented along the hard axis ($\beta = 120^\circ$). The timescale on the horizontal axis denotes the time difference between pump and probe beam. The red curve is a fit using equation 17.	37
5.6	Magnetization oscillations measured with TR-MOKE. The external field of 911Oe is oriented along the hard axis ($\beta = 120^\circ$). The timescale on the horizontal axis denotes the time difference between pump and probe beam. The red curve is a fit using equation 17.	38
5.7	Magnetization oscillations measured with TR-MOKE. The external field of 1138Oe is oriented along the hard axis ($\beta = 120^\circ$). The timescale on the horizontal axis denotes the time difference between pump and probe beam. The red curve is a fit using equation 17.	38
5.8	Precession frequency as a function of the external field measured for an external field angle $\beta = 120^\circ$. The red line represents the fit using equation 23 with the parameters given in table 5.1.	39
5.9	Precession frequency as a function of the external field measured for an external field angle $\beta = 20^\circ$. The red line represents the fit using equation 23 with the parameters given in table 5.1.	40

5.10	Precession frequency as a function of the external field angle β measured for an external field value $H_{ext} = 458 Oe$. The red line represents the fit using equation 23 with the parameters given in table 5.1.	40
5.11	Precession frequency as a function of the external field angle β measured for an external field value $H_{ext} = 685 Oe$. The red line represents the fit using equation 23 with the parameters given in table 5.1.	41
6.1	Gilbert damping as a function of the external field. The field is oriented along the hard axis ($\beta = 120^\circ$). The red curve represents the derivative of the magnetization's equilibrium angle with respect to H_{ext}	46
6.2	Gilbert damping as a function of the external field. The field angle is $\beta = 20^\circ$. The red curve represents the derivative of the magnetization's equilibrium angle with respect to H_{ext}	47
6.3	Gilbert damping as a function of the external field angle β with $H_{ext} = 458 Oe$. The red curve represents the derivative of the magnetization's equilibrium angle with respect to β	47
6.4	Gilbert damping as a function of the external field angle β with $H_{ext} = 485 Oe$. The red curve represents the derivative of the magnetization's equilibrium angle with respect to β	48
6.5	Gilbert damping as a function of the precession frequency. The external field angle, β , is fixed to 120° and 20° for the black and red curve, respectively. The frequency is varied by changing the external field H_{ext} . The two lines are linear fits to the data.	49
6.6	Gilbert damping as a function of the precession frequency. The external field value, H_{ext} , is fixed to $685 Oe$ and $458 Oe$ for the green and blue curve, respectively. The frequency is varied by changing the external field angle β . The two curves are first order exponential fits to the data.	50
6.7	Gilbert damping parameter as a function of the frequency for three different Ni samples. The frequency is varied by a variation of the applied field.	51

Table:

5.1	Overview on the parameters of equation 23.	43
-----	---	----

Magnetization Dynamics and Anisotropy in
Ferromagnetic/Antiferromagnetic Ni/NiO Bilayers

1 Introduction

Magnetism is one of the key phenomena used in modern information technology. Beside the magnetic remanence which is the backbone of all magnetic, non – volatile data storage, other magnetic effects are essential for modern devices. These effects can be observed in a variety of multilayer structures, made of different combinations of ferromagnetic (FM), nonmagnetic and antiferromagnetic (AFM) materials. The technically most important of these effects is the Giant Magnetoresistance (GMR), discovered in 1988 [1, 2]. GMR is observed in structures of alternating ferromagnetic and non magnetic layers. It causes a large change in the material's resistance, when the relative orientation of the magnetic moments in the ferromagnetic layers is changed from parallel to antiparallel. This technique finds applications in magnetic random access memory (MRAM) as well as in magnetic field sensors or hard drive read heads. In fact, without GMR, the current data densities on hard drives would not be possible. Another area of great interest is the field of FM/AFM multilayers. These systems exhibit a unique type of anisotropy called exchange bias (EB) [3]. EB acts as a pinning mechanism in modern GMR devices and it can be used to achieve data densities, higher than what is allowed by the superparamagnetic limit [4].

High data densities are important, but relatively useless without a fast mechanism to write the data, i.e., to manipulate the magnetization. In order to switch the magnetization at rates in the GHz regime, necessary for modern computer applications, it is crucial to understand dynamic magnetization processes. A relatively novel all-optical pump probe technique can resolve those dynamic processes in the time domain with

picosecond resolution [5]. These time domain measurements provide direct information about intrinsic spin damping, which is a key factor to design fast memory devices.

The goal of this thesis is to use this pump probe technique to study magnetization dynamics and damping in a Ni/NiO film as an example for a FM/AFM interface.

The main objectives are:

- Characterize the anisotropy by measuring the angle dependence of coercivity and exchange bias
- Measure the magnetization precession frequency as a function of external field and as a function of the angle between external field and the anisotropy axes
- Determine the anisotropy constants by fitting these angle and field dependences
- Study the intrinsic damping as a function of field, frequency and angle

Chapter 2 of this thesis discusses the theory of the magneto-optical Kerr effect (MOKE), the magneto-crystalline anisotropy and the theoretical description of magnetization dynamics. The experimental setup and the sample used are described in chapter 3. Results and discussion of the different measurements are presented in chapters 4, 5 and 6. Chapter 7 contains the conclusions.

2 Theory

2.1 Magneto Optical Kerr Effect - MOKE

The Kerr Effect is named after the Scottish physicist John Kerr, who discovered in the late nineteenth century that linearly polarized light changes its polarization upon reflection off a magnetized medium. This effect is similar to the Faraday Effect, where the polarization is rotated while the light is transmitted through a Faraday active material in the presence of a magnetic field. The Kerr effect is explained in terms of the material's dielectric tensor, $\vec{\epsilon}$, which is diagonal in an isotropic medium. Either an applied magnetic field or an effective magnetization of the medium changes the isotropy of the material and adds off-diagonal elements to $\vec{\epsilon}$, which are proportional to the magnetization [6]. The dielectric tensor can be written as [7]:

$$\vec{\epsilon} = \epsilon_0 \begin{pmatrix} 1 & iQ_z & -iQ_y \\ -iQ_z & 1 & iQ_x \\ iQ_y & -iQ_x & 1 \end{pmatrix}. \quad (1)$$

The normal modes of light are left and right polarized with refraction index

$$n_{L,R} = \sqrt{\epsilon_0} \left(1 \mp \frac{1}{2} \vec{Q} \cdot \hat{k} \right), \quad (2)$$

where $\vec{Q} = (Q_x, Q_y, Q_z)$ is called the Voigt vector, and \hat{k} is the unit vector along the direction of light propagation.

Equation 2 causes real and imaginary parts of the refractive index, n , to be different for left and right (LCP and RCP) circular polarized light. Linear polarized light

can be described as a sum of LCP and RCP components, with the same frequency and amplitude. Therefore, variations in the real part of n cause a phase difference between LCP and RCP components and lead to a rotation of the polarization denoted as the Kerr angle ρ . Differences in the complex part of n are responsible for a difference in reflectivity and therefore affect the magnitude of the two components. This gives rise to an elliptical polarization of the light called the Kerr ellipticity η [8]. A schematic of this process is shown in figure. 2.1.

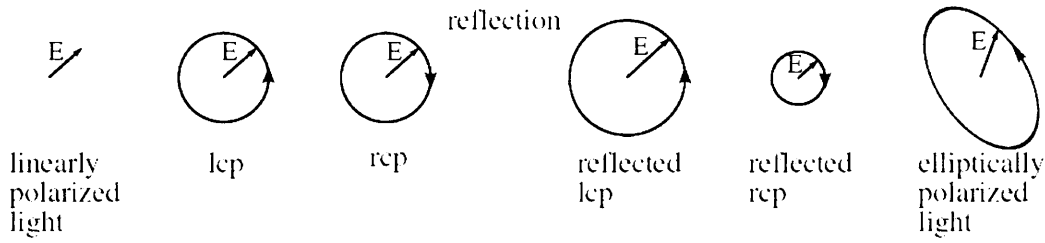


Figure 2.1: Schematic of the Kerr effect. The incoming linearly polarized light can be decomposed into LCP and RCP components which have different amplitudes and phases after reflection from a magnetic medium. This leads to an ellipticity and a rotation of the polarization. Figure taken from ref. [9]

One distinguishes between three main MOKE geometries depending on the orientation of the magnetization relative to the surface of the sample and to the plane of incidence. The polar MOKE geometry measures the magnetization component that is perpendicular to the plane of the sample and in the plane of incidence. For the longitudinal and the transverse MOKE geometries, the magnetization component parallel to the plane of the sample is measured. In the longitudinal case, the measured magnetization component is also parallel to the plane of incidence while in the transverse setup it is perpendicular to the plane of incidence. The three geometries are shown in figure. 2.2.

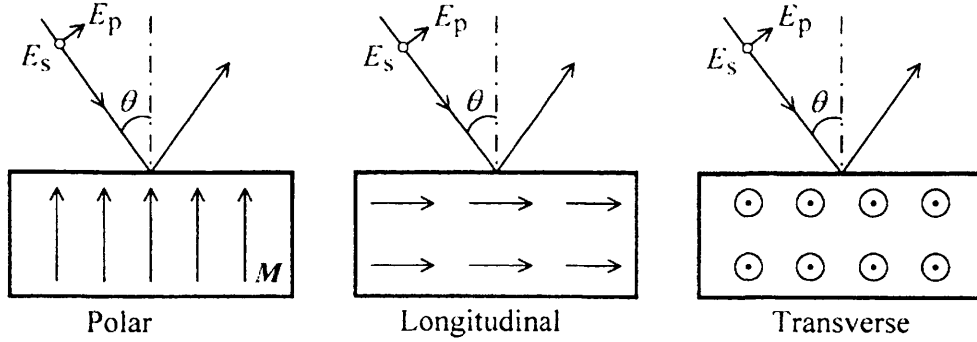


Figure 2.2: Sketch of the three main MOKE geometries. They are determined by the orientation of the magnetization with respect to the surface of the sample and to the plane of incidence. The light can be either polarized perpendicular (s) or parallel (p) to the plane of incidence. Figure taken from ref. [8]

In contrast to longitudinal and polar geometry, the transverse MOKE does not rotate the polarization, instead the reflectivity of the sample depends on \overline{M} . This means, that the transverse component can not be measured with the cross polarization scheme used in this thesis. For the other two MOKE geometries, the effective Kerr rotation depends on the angle of incidence. Figure 2.3 shows the cross-polarization factor for longitudinal MOKE. It is a measure of the conversion efficiency from p to s polarized light upon reflection, as a function of the angle of incidence, θ , as shown in figure 2.2 [8]. The maximum Kerr response can be achieved for $\theta \approx 65^\circ$. For polar MOKE, the cross-polarization factor is nearly constant for $0^\circ < \theta < 60^\circ$ and goes to zero for $\theta = 90^\circ$. In the apparatus used in this thesis, experimental constraints limit $\theta \approx 45^\circ$, however this value still guarantees a good MOKE response for both longitudinal and polar geometries. Note that the polar MOKE response is typically an order of magnitude stronger than its longitudinal counterpart.

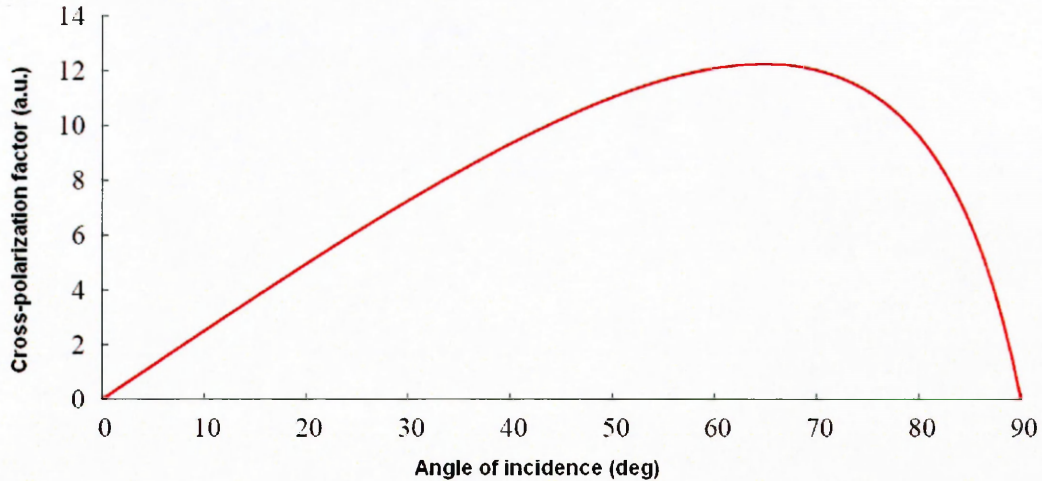


Figure 2.3: The cross-polarization factor for longitudinal MOKE as a function of the angle of incidence. The highest Kerr response can be achieved at an incidence angle of roughly 65°. Figure adapted from ref. [9]

2.2 Demagnetizing Fields

In a magnetized body, there exists a natural field trying to demagnetize the body. Uncompensated magnetic poles at the boundaries of a finite, magnetized material create an effective field that acts to frustrate the magnetization. This important effect is shown in figure 2.4 [10].

It is described by a demagnetizing field, H_d , which is proportional to the magnetization because it determines the number of free poles.

$$\vec{H}_d = -N\vec{M} \quad (3)$$

N is called the demagnetization factor and depends only on the shape of the sample. It can be calculated for an ellipsoid with its three principal axes a , b and c shown in figure 2.5 (a) [11].

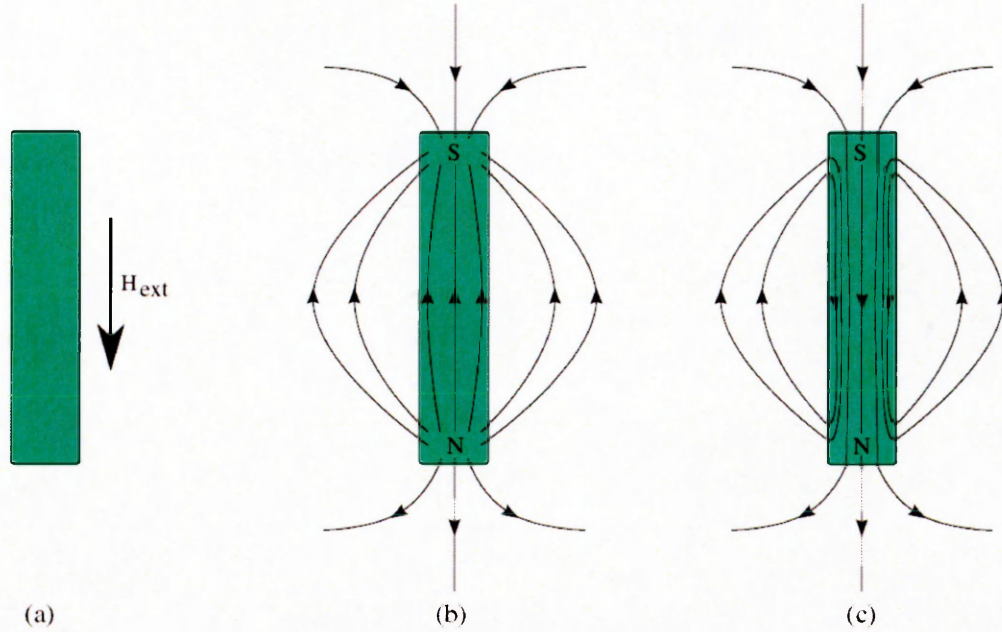


Figure 2.4: (a) shows a bar magnet in an external field H_{ext} . This field causes the poles and their field lines shown in (b). Those field lines are pointing in the opposite direction of the external field and causing the demagnetization of the sample. The effect decreases with increasing distance between the two poles. (c) shows the effective B field with its closed field lines. Inside the magnet, it still points in the direction of the former external field H_{ext} because the demagnetization field can never exceed the magnetization in magnitude. Figure taken from ref. [9]

In this case, N_a, N_b and N_c are the demagnetizing factors along these three axes. If

$a \neq b = c$ and in the limit $\frac{c}{a} \rightarrow \infty$ (thin disc), the demagnetization factors in cgs units are

given by

$$N_a \approx 4\pi \quad \text{and} \quad N_b = N_c = 0. \quad (4)$$

This means that for a thin film the magnitude of the demagnetization field is

$$H_d = 4\pi M \cos \theta, \quad (5)$$

where θ is the out of plane angle of the magnetization vector. This field acts to pull \overline{M} in the direction of the plane. (In SI units $N_a \approx 1$ and $N_b = N_c = 0$.)

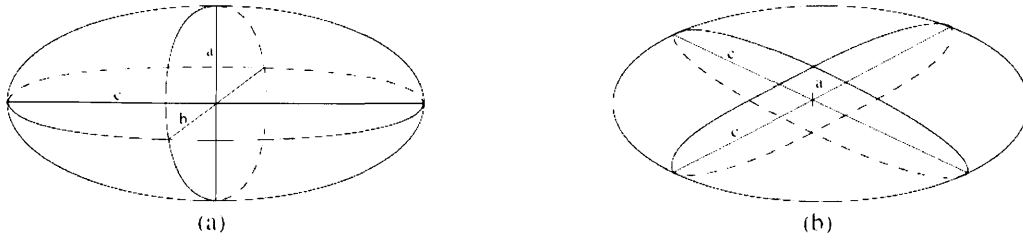


Figure 2.5: (a) shows a general ellipsoid with its axes a , b and c . If the axes b and c have the same length as in (b) it is called oblate spheroid. This can be considered a thin film in the limit $c \rightarrow \infty$. Figure taken from ref. [11].

2.3 Magnetocrystalline Anisotropy

The response of the magnetic properties of a material, such as the coercivity and hysteresis, in general depends on the direction of an applied external field. This effect is caused by the crystallographic structure and is called magnetic anisotropy [10]. It can be described by an anisotropy energy, whose minima correspond to the preferred direction of magnetization. These energetically favorable directions are called easy axes of magnetization, whereas the directions corresponding to maxima in the energy are called hard axes of magnetization. The sample used in this thesis is made of nickel, which has a face centered cubic (fcc) structure. For cubic materials, it is common to express the anisotropy energy in terms of the direction cosines $(\alpha_x, \alpha_y, \alpha_z)$ of the magnetization vector with respect to the cube edges.

For example, α_x denotes the cosine of the angle between the magnetization vector and the x direction. In spherical coordinates the α_i are given by

$$\begin{aligned}\alpha_x &= \sin \theta \cos \phi, \\ \alpha_y &= \sin \theta \sin \phi, \\ \alpha_z &= \cos \theta.\end{aligned}\tag{6}$$

The high cubic symmetry requires that the energy expansion does not include odd powers of α_i , because a change of sign in any α_i leads to a direction equivalent to the original one. Furthermore, the energy must be invariant under the exchange of any two α_i . These facts, with the additional requirement that $\alpha_x^2 + \alpha_y^2 + \alpha_z^2 = 1$ yields a general expression for the cubic energy [10]:

$$E_{cubic} = K_1 (\alpha_x^2 \alpha_y^2 + \alpha_y^2 \alpha_z^2 + \alpha_z^2 \alpha_x^2) + K_2 (\alpha_x^2 \alpha_y^2 \alpha_z^2) + K_3 (\dots) + \dots\tag{7}$$

The coefficients K_i are called anisotropy constants and are unique to specific materials. For most materials the bulk values of K_1 and K_2 are known. Higher order terms in most cases are small and cannot be determined reliably.

The crystallographic orientation of the easy axes in a cubic material depends on the sign of its anisotropy constants. In the case $K_1 > 0$, which is the case for iron, the easy axes are [100], [010] and [001] as shown in figure 2.6 (left). For $K_1 < 0$, which we have in nickel, the easy axes are [111], [-1,1,1], [1,-1,1] and [1,1,-1]. (fig. 2.6 (right))

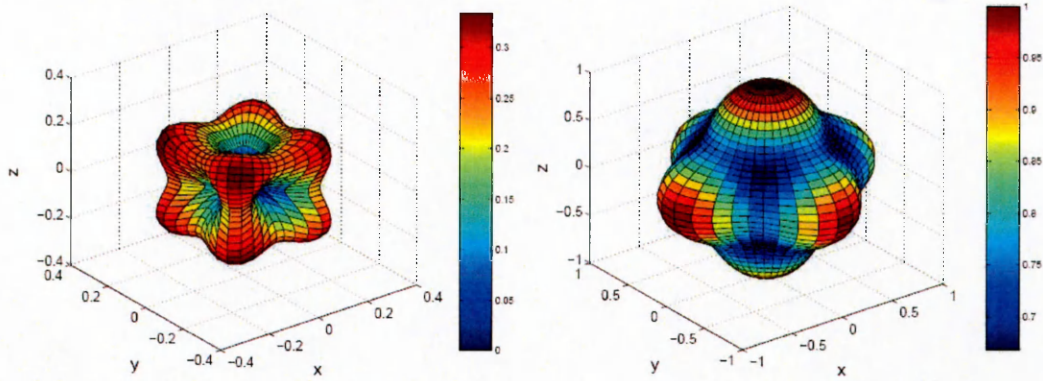


Figure 2.6: Polar plot of the cubic anisotropy energy density (Eq. 7). The left plot represents the case $K_1 > 0$. Here the easy axes are along the cube edges as in the case of iron. The right plot shows the case for $K_1 < 0$. In such a material, like nickel, the easy axes are along the cube diagonals. Figure taken from ref. [12].

2.4 Magnetization Dynamics

A magnetic field \vec{B} exerts a torque $\vec{\tau}_i$ on the magnetic moments $\vec{\mu}_i$ in a material.

$$\vec{\tau}_i = \vec{\mu}_i \times \vec{B} \quad (8)$$

In the macroscopic limit, it is more convenient to use the magnetization \vec{M} instead of $\vec{\mu}$.

The magnetization is the volume density of the magnetic moment:

$$\vec{M} = \frac{\sum_i \vec{\mu}_i}{V} \quad (9)$$

The equation of motion for the magnetization in an external magnetic field \vec{H} is [13]

$$\frac{d\vec{M}}{dt} = -\gamma \vec{M} \times \vec{H}. \quad (10)$$

In this equation, γ is the gyromagnetic ratio. It is defined as

$$\gamma = \frac{g|e|\hbar}{2m_e c} = g \cdot 8.79 \cdot 10^6 \frac{\text{Hz}}{\text{Oe}} \text{ (cgs) or}$$

$$\gamma = \frac{g\mu_0 |e|}{2m_e} = g \cdot 87.9 \cdot 10^9 \frac{\text{Hz}}{\text{Am}^{-1}} \text{ (SI)}. \quad (11)$$

Typically, the dimensionless g-factor or spectroscopic splitting factor has a value close to two, but for some ferromagnetic materials its value is higher. In the case of Nickel $g = 2.21$. [10]

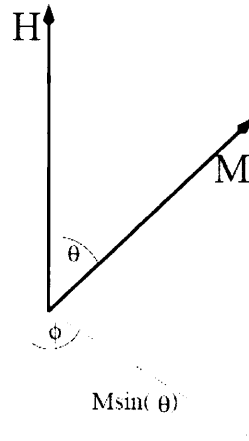


Figure 2.7: The undamped magnetization vector precesses around the effective magnetic field. ϕ and θ are the azimuthal and polar angles of \vec{M} respectively. Figure taken from ref. [9].

According to equation 10 the magnetization, once excited, precesses indefinitely around the direction of the magnetic field. In order to describe real systems, Gilbert (1955) proposed a phenomenological viscous damping term [14]. Equation 10 becomes

$$\frac{d\vec{M}}{dt} = -\gamma \vec{M} \times \left(\vec{H} - \eta \frac{d\vec{M}}{dt} \right). \quad (12)$$

In this form, the Landau Lifshitz Gilbert (LLG) equation is not easy to solve for \vec{M} , however, we can simplify it by considering the inner product of \vec{M} with $\frac{d\vec{M}}{dt}$:

$$\vec{M} \cdot \frac{d\vec{M}}{dt} = \frac{1}{2} \frac{d}{dt} (\vec{M})^2 \equiv 0. \quad (13)$$

Thus, the magnitude of \vec{M} , M_s , is a constant of motion. Only homogeneous damping processes that leave \vec{M} constant can be described by the Gilbert formalism. If we consider the outer product $M \times \frac{d\vec{M}}{dt}$, we have

$$M \times \frac{d\vec{M}}{dt} = -\gamma \vec{M} \times (\vec{M} \times \vec{H}) - \gamma \eta |\vec{M}|^2 \frac{d\vec{M}}{dt}, \quad (14)$$

which, substituted into equation 12 yields

$$\frac{1 + \alpha^2}{\gamma} \frac{d\vec{M}}{dt} = -\vec{M} \times \vec{H} - \frac{\alpha}{M_s} \vec{M} \times (\vec{M} \times \vec{H}), \quad (15)$$

where $\alpha \equiv \gamma \eta M_s$. This unitless parameter is called the Gilbert damping parameter.

Figure 2.8 is a sketch of the damped precessional motion emphasizing the components of equation 15.

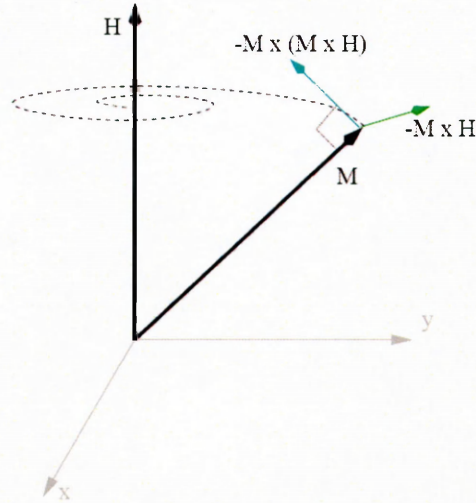


Figure 2.8: The magnetization vector precesses according to equation 15. $-\vec{M} \times \vec{H}$ is always perpendicular to \vec{M} and \vec{H} . It causes the precession around \vec{H} whereas $-\vec{M} \times (\vec{M} \times \vec{H})$ causes the damping by pulling the magnetization in the direction of \vec{H} . Figure taken from ref. [9]

For small oscillations, the LLG equation is linearized, yielding solutions as an exponentially damped sine with a decay time τ and frequency ω [15, 16].

$$A \cdot e^{-t/\tau} \cdot \sin(\omega t + \delta) \quad (16)$$

The Gilbert damping parameter, α , can be extracted from these fits using the relation

$\alpha = \frac{1}{\omega\tau}$ [17]. The decay time, τ , is just a measure for the time it takes to damp out the

oscillations while α represents the damping per oscillation. α therefore determines the number of oscillations after an excitation. Figure 2.9 shows equation 16 for different values of α at a certain frequency.

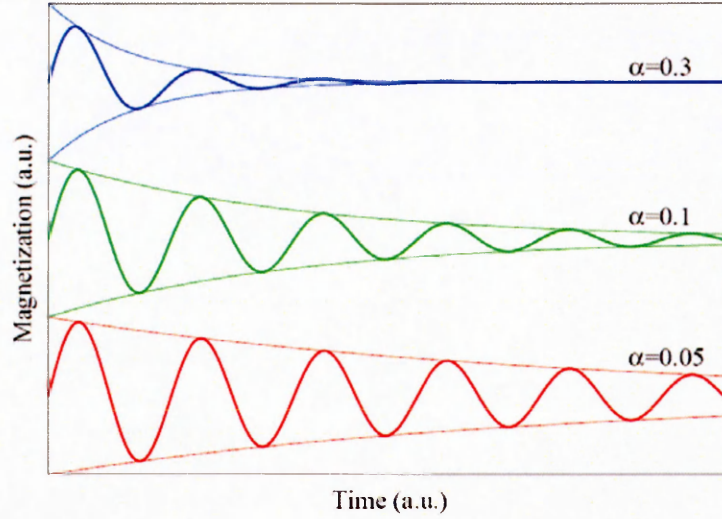


Figure 2.9: Plots of equation 16 for different values of α . Figure taken from ref. [9].

In real pump probe measurements, non magnetical effects like electron lattice interactions cause deviations between measured oscillations and equation 16. To take this into account, a first order correction in form of a linear term is added to equation 16. It becomes

$$A \cdot e^{-\frac{t}{\tau}} \cdot \sin(\omega t + \delta) + B + m t . \quad (17)$$

2.5 Ferromagnetic Resonance Frequency

The resonance frequency for a system obeying equation 10 can be determined analytically under the assumption of small oscillations of the magnetization around its equilibrium position. In spherical coordinates, equation 10 takes the form

$$\frac{d\theta}{dt} = \gamma \cdot H_{\phi} \quad \text{and} \quad \frac{d\phi}{dt} = -\frac{\gamma}{\sin\theta} \cdot H_{\theta} , \quad (18)$$

where H_ϕ and H_θ are the ϕ and θ components of the effective magnetic field, \vec{H}_{eff} , in spherical coordinates. The effective field is defined as

$$\vec{H}_{eff} = -\frac{dF}{d\vec{M}} = -\vec{\nabla}_M \cdot F \quad (19)$$

where F is the free energy density of the system. \vec{H}_{eff} contains the external field, the demagnetization field and other crystalline anisotropy fields. \vec{H}_{eff} can be written as

$$\vec{H}_{eff} = (H_M, H_\theta, H_\phi) = \left(-\frac{dF}{dM_s}, -\frac{1}{M_s} \frac{dF}{d\theta}, -\frac{1}{M_s \cdot \sin\theta} \frac{dF}{d\phi} \right) \quad (20)$$

Assuming small oscillations around the equilibrium position, the energy can be expanded as a power series up to second order. In this case the derivatives with respect to θ and ϕ are

$$\frac{\partial F}{\partial \theta} = \frac{\partial^2 F}{\partial \theta^2} \delta\theta + \frac{\partial^2 F}{\partial \theta \partial \phi} \delta\phi \quad \text{and} \quad \frac{\partial F}{\partial \phi} = \frac{\partial^2 F}{\partial \phi^2} \delta\phi + \frac{\partial^2 F}{\partial \theta \partial \phi} \delta\theta \quad (21)$$

Combining equations 18, 20 and 21 yields a system of linear equations,

$$\begin{aligned} -\frac{M_s \cdot \sin\theta}{\gamma} \frac{d\theta}{dt} &= \frac{\partial^2 F}{\partial \theta \partial \phi} \delta\theta + \frac{\partial^2 F}{\partial \phi^2} \delta\phi \\ \frac{M_s \cdot \sin\theta}{\gamma} \frac{d\phi}{dt} &= \frac{\partial^2 F}{\partial \theta \partial \phi} \delta\phi + \frac{\partial^2 F}{\partial \theta^2} \delta\theta \end{aligned} \quad (22)$$

which has periodic solutions of the form $\theta, \phi \sim e^{i\omega t}$ if the determinant is equal to zero.

$$\omega = \frac{\gamma}{M_s \cdot \sin\theta} \sqrt{\frac{\partial^2 F}{\partial \theta^2} \frac{\partial^2 F}{\partial \phi^2} - \left(\frac{\partial^2 F}{\partial \theta \partial \phi} \right)^2} \quad (23)$$

This formula is known as the Smit – Suhl formula [18, 19].

In the following chapters, the geometry of the sample and the angles ϕ and θ are defined as follows (fig. 2.7):

- The plane of the sample lies in the x-y plane.
- The x axis points in the direction of the free energy's global minimum. This direction is called easy axis.
- ϕ denotes the angle between the in plane component of \vec{M} and the easy axis.
- θ is the angle between \vec{M} and the z-axis.

3 Experimental Setup

Two different measurement techniques are used in this thesis: static MOKE (S-MOKE) and time resolved pump probe MOKE (TR-MOKE). S-MOKE is used to measure the sample magnetization as a function of the applied magnetic field, and TR-MOKE makes it possible to resolve magnetization dynamics on the picosecond timescale. Both setups are discussed in this chapter.

3.1 S-MOKE

Fig. 3.1 shows a schematic of the MOKE setup used in this thesis. The sample is mounted on a rotation stage (Newport SR 50) oriented between the poles of an electromagnet (GMW 3470) such that applied fields are constrained to the plane of the sample. This makes it possible to apply the external field at any in-plane angle with respect to the sample's crystallographic axes. It allows one to obtain information about the angular dependence of the sample anisotropy. A He-Ne Laser (Melles Griot 25 LHR) with a wavelength of 632.8nm is directed at the sample and polarized by a Glan polarizer (Newport 10GL08) such that the ingoing polarization is in the plane of incidence. Reflected light is directed to a second Glan polarizer oriented nearly 90° from the first one. Finally, the outgoing beam is focused via a lens on a photodiode (Thor Labs DET 210). The laser is modulated at $\sim 280\text{Hz}$ with a chopper and a lock-in amplifier (SR 530) filters out all other frequency components thus eliminating much of the noise. An external computer controls the rotation stage, the electromagnet acquires the data. The best signal is measured if the relative angle between polarizer and analyzer is chosen to

be half a degree to one degree off the extinction angle. All measurements are performed at room temperature. Note that because of the high demagnetization fields only the component of magnetization that is parallel to both the plane of incidence and the plane of the sample contributes to the MOKE signal. Therefore the longitudinal MOKE geometry, described in chapter 2.1 is realized.

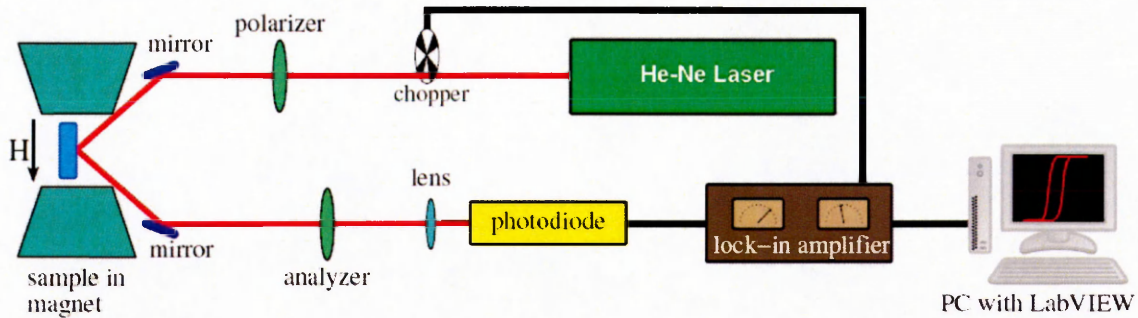


Figure 3.1: Schematic of the static MOKE setup. A polarizer analyzer combination is used to measure the polarization rotation due to the magnetization in the sample. Figure adapted from ref. [9]

3.2 TR-MOKE

In order to perform time resolved measurements, the setup has to be modified. It is shown in figure 3.2. Instead of the He-Ne Laser, an amplified Ti:Sapphire laser system (Spectra Physics Tsunami and Spitfire) with a wavelength of 800nm, generates 150fs laser pulses at 1kHz repetition rate. Its average power output is 700mW and the peak power 4.7GW. After collimating the beam with a telescope, it is split into a pump beam and a probe beam by a beam splitter. The probe beam is polarized parallel to the plane of incidence and attenuated such that its average power is approximately 5mW before it reaches the sample. The pump beam is directed through a computer controlled delay stage, which provides a time delay between the two beams such that the probe beam arrives after the

pump beam. The pump beam power before reaching the sample is 50mW. A modulation scheme is used to filter out unwanted signals: in this case the pump beam is modulated at $\sim 280\text{Hz}$ with a chopper and the lock-in amplifier accepts only this frequency component of the probe beam. Both beams are directed on the same spot on the sample. The diameters of the pump and probe beam are $(2.0 \pm 0.1)\text{mm}$ and $(1.6 \pm 0.1)\text{mm}$ respectively. These beam sizes contain 50% of the beams total power. A PC with a LabView program controls the experiment and records the data. In contrast to the S-MOKE measurement, the TR-MOKE signal is mainly caused by the component of magnetization that is parallel to the plane of incidence and perpendicular to the plane of the sample. Therefore the polar geometry described in chapter 2.1 is realized. Like S-MOKE, the TR-MOKE experiments are also performed at room temperature.

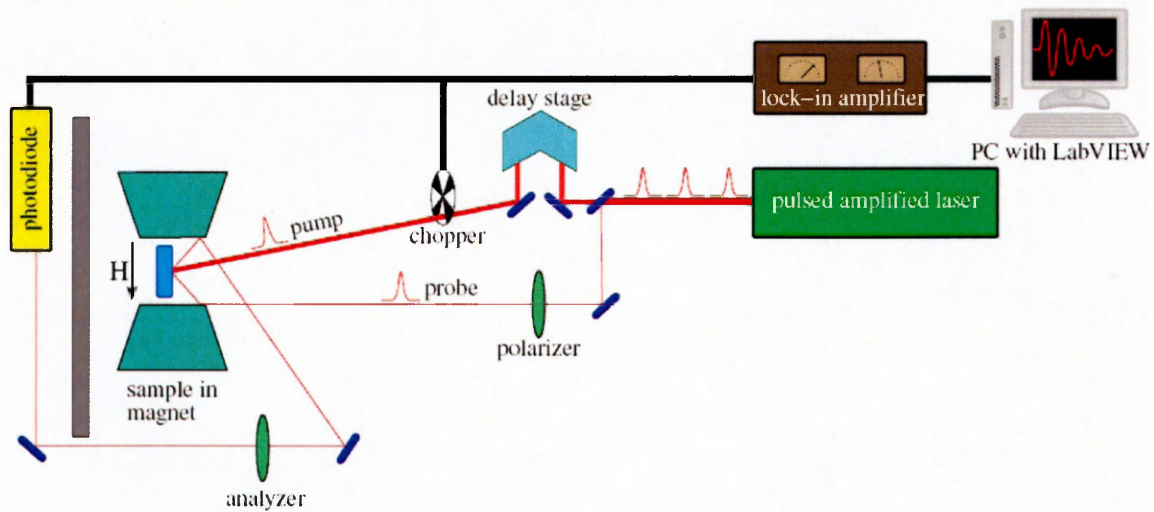


Figure 3.2: Schematic of the TR-MOKE experimental setup. The path length of the pump beam can be altered via a delay stage, causing the pump beam to arrive at the sample some time Δt before the probe beam. The magnetization oscillations excited by the pump beam are measured with the polarizer analyzer setup. The MOKE signal is recorded as a function of Δt . Figure taken from ref. [9]

3.3 Sample

The sample used was grown by the group of Prof. R.A. Lukaszew at the University of Toledo. This group published a paper containing detailed information about the sample [20].

Important aspects for this thesis are described below.

The Ni film was grown on MgO (001) substrate using MBE. It was in situ annealed in UHV at 573K (~1/3 of Ni melting temperature) for several hours [20]. The total film thickness is reported to be 30nm (~170 monolayers). Transmission electron microscopy (TEM) and reflection high energy electron diffraction (RHEED) studies performed during growth and after in situ annealing, indicate the formation of a rough interfacial layer of NiO (~7-8nm thick) caused by the annealing process. The origin of this interfacial layer, which is shown in figure 3.3, can be inferred from the crystalline structure of the substrate and the film. Nickel and MgO both have fcc structure but their lattice parameters differ by 16.4%, whereas the lattice parameter of NiO, which also has fcc structure, only differs by 0.9% from that of MgO. (The lattice parameters of Ni, MgO and NiO are 3.52Å, 4.213Å and 4.177Å respectively.) As a result of this lattice mismatch, a NiO layer is formed to relieve the strain due to the lattice mismatch between Ni and MgO [20]. After this thin intermediate layer is formed the crystal field of the (001) MgO substrate favors the subsequent cube on cube epitaxial Ni growth observed, but with high defect density [20].

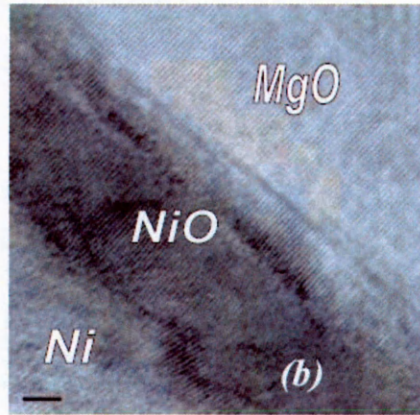


Figure 3.3: Cross sectional TEM image of the sample after in situ annealing. The dark area between Ni and MgO is a 7-8 nm thick NiO layer. It forms during growth of the sample and becomes thicker during further annealing. The bottom left scale corresponds to two nanometers. Figure taken from ref.[20]

In a material with a cubic structure like nickel, the magnetic anisotropy is expected to be fourfold. To verify this, longitudinal magneto optical Kerr effect (MOKE) has been used to study the anisotropy in the magnetization reversal on the samples prior and after in situ annealing [20]. Figure 3.4(a) shows the azimuthal dependence of the coercivity prior to annealing. Here the fourfold symmetry is clearly visible. However, after annealing the fourfold symmetry is broken, as the coercivity exhibits an additional uniaxial component as shown in figure 3.4(b).

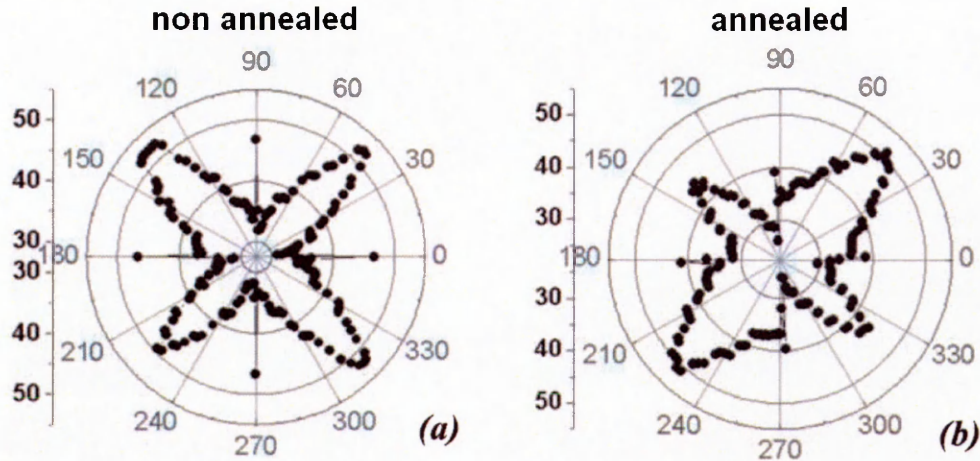


Figure 3.4: Azimuthal dependence of the coercivity for the as grown sample (a) and after in situ annealing (b). The as grown sample exhibits the expected cubic four fold symmetry. The annealing process induces an additional uniaxial anisotropy. The vertical axis corresponds to the coercive field in Oe. Figure taken from ref. [20]

This uniaxial anisotropy is consistent with prior reports about a lattice distortion in NiO along [111] causing such an anisotropy [20]. The annealing process causes a tetragonal lattice distortion, manifested as a uniaxial anisotropy component [20]. Furthermore, a weak, but measurable, exchange bias field of 16 Oe is reported in ref. [20].

3.4 Anisotropy Energy

The information provided in this chapter, makes it possible to write down a more specific expression for the anisotropy energy of the sample. The anisotropy should be based on the cubic anisotropy of nickel. In addition, there should be a tetragonal and a uniaxial anisotropy term to take into account the tetragonal lattice distortions and the uniaxial component measured in static MOKE, respectively. Therefore the anisotropy energy is assumed to be the sum of a cubic, a tetragonal and a uniaxial term.

$$E_{anisotropy} = E_{cubic} + E_{tetragonal} + E_{uniaxial} \quad (24)$$

For the cubic and the uniaxial energy, only an in plane dependence is considered because their out of plane components can be neglected, due to the strong demagnetization field.

The cubic energy expression for the (001) plane is given by equation 7. Setting $\theta = \frac{\pi}{2}$ it

becomes

$$E_{cubic} = \frac{KI}{4} \cos(2\phi)^2 \quad (25)$$

The expression for the in plane uniaxial anisotropy energy is

$$E_{uniaxial} = UI \sin(\phi)^2 \quad (26)$$

In contrast to the other two energy terms, the tetragonal term has a significant out of plane (perpendicular) contribution [21].

$$E_{tetragonal} = E_{in\ plane} + E_{perp} = \frac{TI}{4} \cos(2\phi)^2 + T_{perp} \cos(\theta)^2 \quad (27)$$

The anisotropy constants KI , UI , TI and T_{perp} are determined from the TR-MOKE data in chapter 5.

4 Static MOKE

4.1 Measurements

Static MOKE measurements are used to investigate the angular dependence of the sample's anisotropy. Using this information, in combination with the dynamic measurements described in chapter 5, it is possible to determine the sample's anisotropy constants. To obtain the angular dependence of the anisotropy, the magnetization of the sample as a function of an applied magnetic field (i.e. a hysteresis loop) is measured for different in-plane angles of the applied field. The field angle, β , takes values between 0° and 360° in steps of 5° . In order to control this angle, the sample is mounted inside the magnet on a rotation stage. For this measurement it is crucial to have the surface of the sample aligned perpendicular to the axis of rotation, otherwise, the reflected beam moves relative to the detector as the sample rotates. A Hall sensor is used to calibrate the magnetic field which is determined to be accurate within ± 5 Oe.

For each field angle four hysteresis loops are recorded and averaged. Figures 4.1 – 4.4 show some of these MOKE loops recorded for characteristic directions. The information extracted from the data is the coercivity field H_C (half width of the loop) and the exchange bias field H_{EB} (the field value the loop is centered around). To obtain these fields, the y-axis is centered about the mean of the two saturation values corresponding to the value where the measured component of magnetization is zero.

$H_C \equiv \frac{1}{2} |H_{C1} - H_{C2}|$ is given by half the difference of the two switching fields (the field

where the magnetization is zero) and $H_{EB} \equiv \frac{1}{2}(H_{C1} + H_{C2})$ is given by their mean, as indicated in figure 4.1.

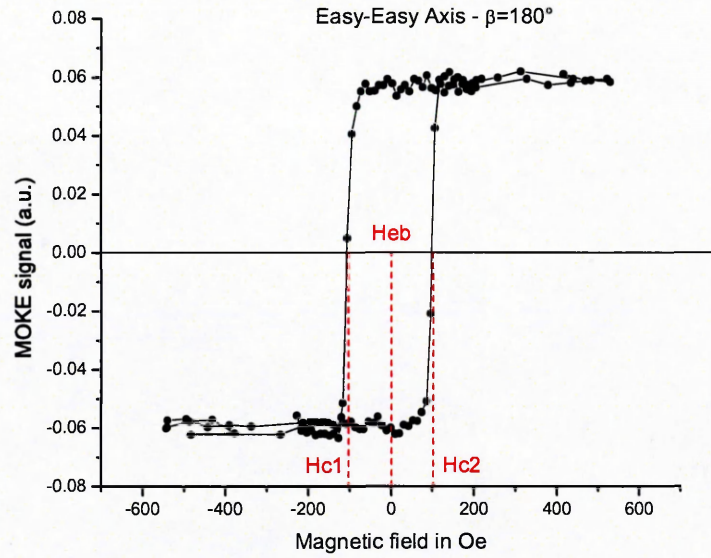


Figure 4.1: Hysteresis loop measured for $\beta = 180^\circ$. H_{C1} , H_{C2} and H_{EB} are indicated by dashed vertical lines.

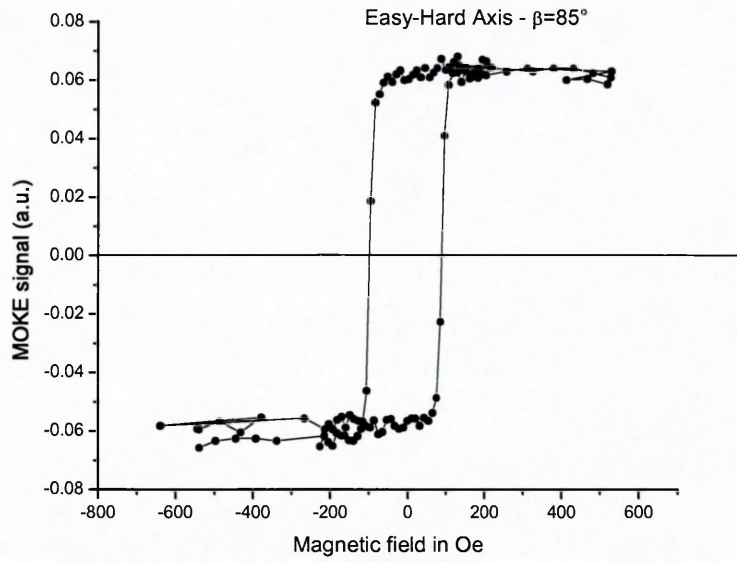


Figure 4.2: Hysteresis loop measured for $\beta = 85^\circ$.

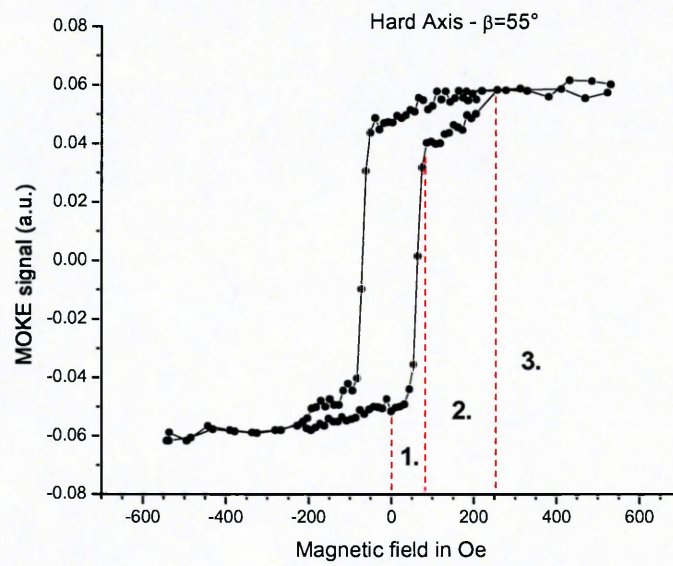


Figure 4.3: Hysteresis loop measured for $\beta = 55^\circ$. 1, 2 and 3 mark the regions of fast switching, slow switching and saturation of the magnetization, respectively.

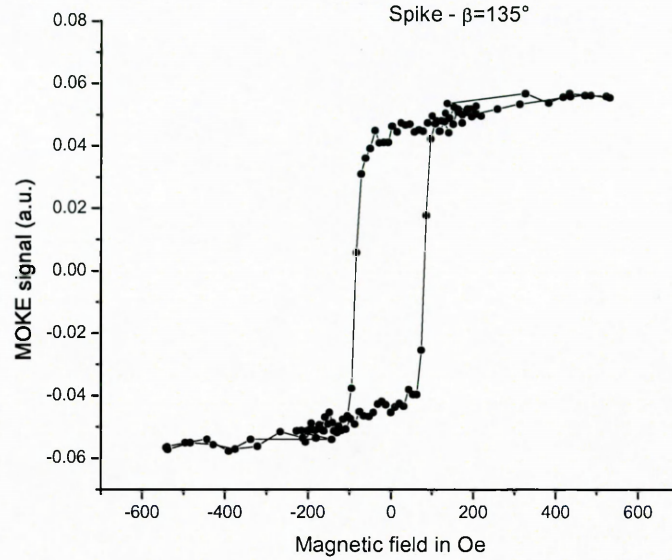


Figure 4.4: Hysteresis loop measured for $\beta = 135^\circ$.

4.2 Results and Discussion

Figure 4.5 shows a polar plot of the measured coercivity field H_C as a function of the external field angle β . The axis where the coercivity is highest (0° and 180°), from now on is referred to as the easy-easy axis (black). If the sample is magnetized in this direction, the free energy, F , is at the lowest value possible. If the sample is magnetized along the second axis (85° and 265°), F is at a local minimum. This axis is called an easy-hard axis (red). The axes where the coercivity is smallest correspond to a maximum in F and are called hard axes (blue). The green direction in figure 4.5 marks a sharp increase in coercivity. These coercivity “spikes” are observed for all $\langle 100 \rangle$ directions. Figure 4.6 shows the four hysteresis loops, corresponding to the highlighted directions.

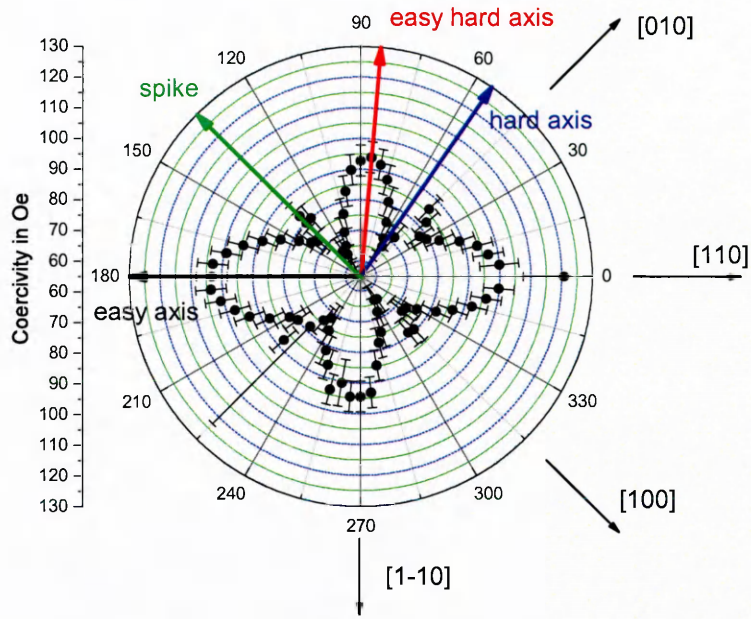


Figure 4.5: Polar plot of the coercivity field H_c as a function of the external field angle β . Also indicated are selected crystallographic directions and the four directions corresponding to the hysteresis loops shown in figure 4.6.

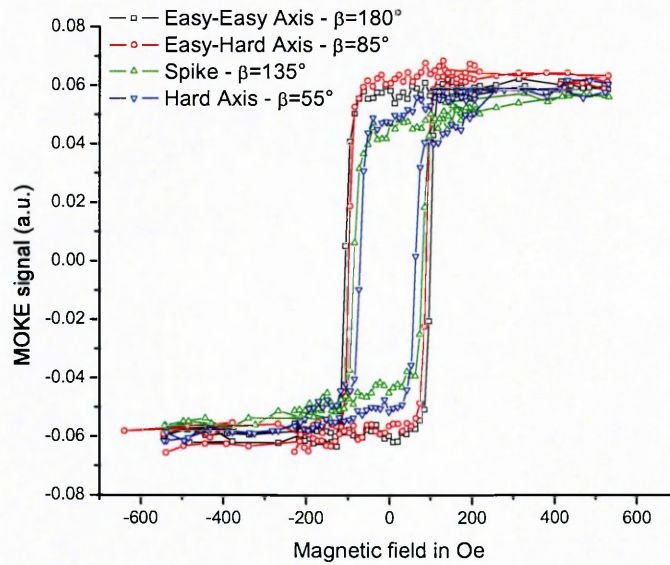


Figure 4.6: Hysteresis loops for the four characteristic directions marked in figure 4.5.

The data indicates the expected cubic fourfold symmetry of nickel with a superimposed uniaxial contribution also observed by Lukaszew et. al. [20] (fig. 3.4 b). As in ref. [20], we notice the presence of four “spikes” (green) located between easy and hard axes at 45° , 135° , 225° and 315° (the angles are defined in the coordinate system, where the easy-easy axis is at 0°). However, the four loops seem to be smoother and less pointed compared to the data published in ref. [20]. It is also interesting to note that, except for the different coercivity values, there is no real difference in the switching behavior of the magnetization for different orientations (fig. 4.1 – 4.4). This behavior is expected because the magnetization is easy to saturate for cubic Ni regardless of the crystallographic direction as can be seen in fig 4.7.

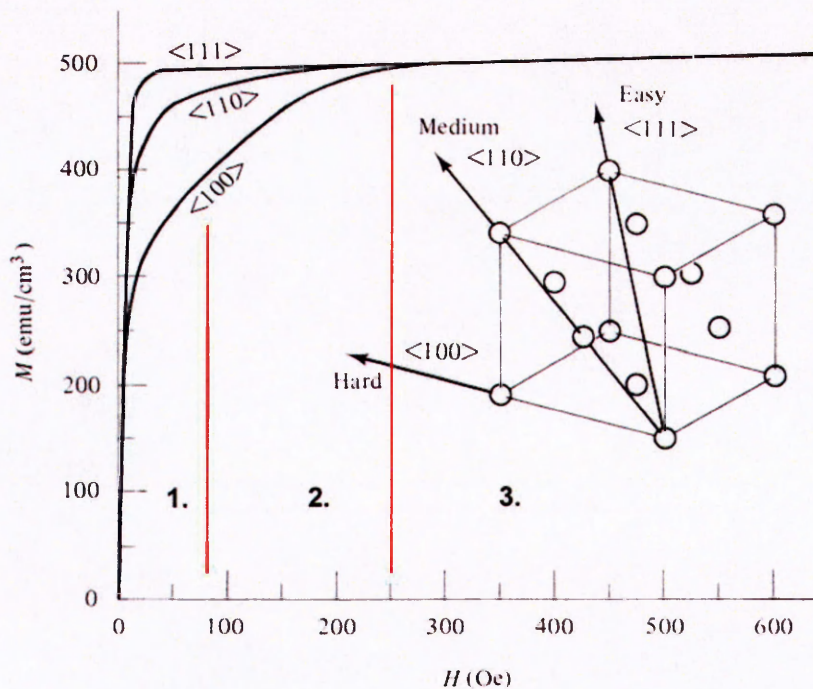


Figure 4.7: Magnetization curves of different crystallographic directions for single crystal nickel. For comparison, the boundaries of region 1, 2 and 3 have the same field value as the regions in figure 4.3. Figure taken from ref. [11].

This is not the case for all ferromagnetic materials. Hexagonal cobalt for example shows totally different magnetization curves (fig. 4.8). Here a field of over 10000 Oe is needed to magnetize the sample along its hard axis which is roughly twenty times the field that is needed to magnetize it along its easy direction. Figure 4.7 also shows the unit cell of Ni and the crystallographic directions, corresponding to easy, hard and intermediate axes of magnetization. The sample, as described in chapter 3, is a MBE grown epitaxial (001) Ni film. Therefore the $\langle 111 \rangle$ easy directions, which represent the global minimum in the cubic anisotropy energy, are pointing out of the sample plane, hence play no roll in the measured in-plane anisotropy. Instead the axes previously called easy-easy and easy-hard axis and pointing in the $\langle 110 \rangle$ directions are identical to the medium axis in figure 4.7 while the in-plane hard axis is identical to the global one. The measured switching behavior of the hard axis can be divided into three regions as depicted in figure 4.3. One can see that the measured saturation region starts exactly at the expected field value of 250 Oe, whereas the region of fast switching, region one, is measured to be a little larger than expected from figure 4.7.

The small exchange bias of 16 Oe that was reported in ref. [20] is not observed in the measurements. This may indicate that the exchange bias degenerates over time.

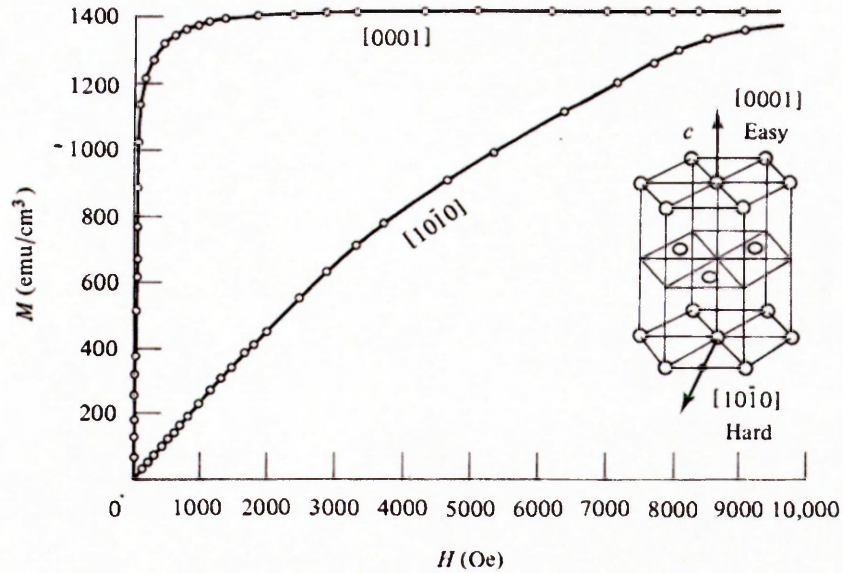


Figure 4.8: Magnetization curves of easy and hard direction for single crystal cobalt. Figure taken from ref. [11]

In summary, the sample quantitatively shows the hysteretic behavior expected for a thick (30nm) Ni (001) film. The angular dependence of the coercivity, a cubic fourfold symmetry with a superimposed uniaxial term, is similar to what was reported in ref. [20]. Note that the angle between easy-easy and easy-hard axis slightly differs from the expected value of 90° . This seems to be a result of the annealing process because it is also present in the original data taken by Lukaszew et. al. [20] after annealing (fig. 3.4 b), but not visible prior to annealing (fig. 3.4 a). The reported exchange bias field of 16 Oe is no longer present in the sample.

5. Time Resolved-MOKE

5.1 Measurements

The time domain response of the magnetization is investigated using the TR-MOKE technique, a relatively novel technique which was introduced by van Kampen et. al. in 2002 [5]. TR-MOKE uses femtosecond laser pulses to excite magnetic spin waves by electronic heating, a process Beaurepaire et. al. described in 1996 [22]. This technique has some advantages of over classical ferromagnetic resonance (FMR) measurements. Compared to the extraction of damping from the line width in frequency domain FMR measurements, TR-MOKE measurements are taken in the time domain, providing direct information about the damping. Furthermore, TR-MOKE is a local technique; it excites and probes the magnetization with a laser beam which limits the spatial resolution to the beam diameter. In the following the laser induced excitation process is described. The excitation is a three step process [5]:

1. Prior to arrival of the pump beam, the magnetization \vec{M} points in the equilibrium direction, ϕ_0 , which lies in the plane of the sample due to the strong demagnetization field. (ϕ_0 is the direction of the effective field $\vec{H}_{eff} = -\vec{\nabla}_M \cdot F$)
2. The pump beam with its peak power of 4.7GW locally heats the sample which changes the sample's anisotropy field, causing \vec{M} to precess around its new equilibrium direction. This process happens on a timescale of 0.5ps [22].

3. The heat diffuses due to electron-phonon interactions and on a time scale of about 10ps the original equilibrium angle is restored. \vec{M} continues to precess around the effective field till it is damped out [5].

Figure 5.1 shows a plot of a typical oscillation. The MOKE signal is plotted as a function of the time difference Δt between pump and probe beam:

$$\Delta t = t_{probe} - t_{pump}$$

The times t_{probe} and t_{pump} correspond to the travel times of the two beams. For $\Delta t < 0$ there is no signal because the probe beam arrives, before the pump beam excites the oscillations. At $\Delta t = 0$ a small peak, the “overlap peak”, is visible indicating the time overlap between the two beams. In this short period of time the three processes described above take place. After that the oscillations begin, whose frequency is given by equation 23. The red curve represents a fit using equation 17.

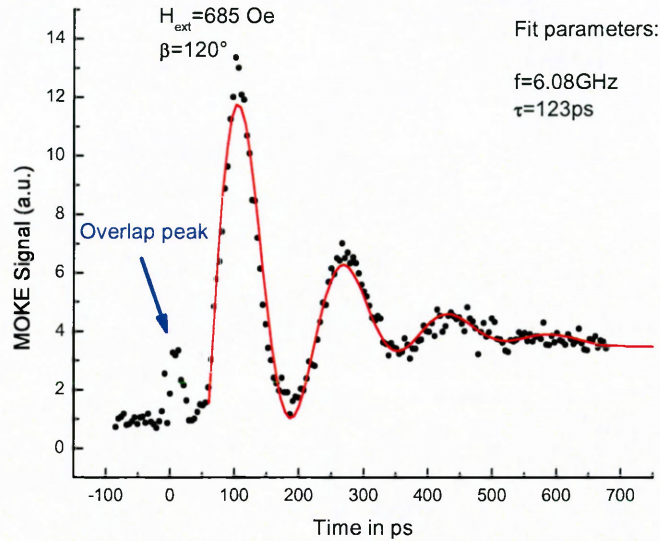


Figure 5.1: A typical magnetization oscillation measured with TR-MOKE. The external field of 685Oe is oriented along the hard axis ($\beta = 120^\circ$). The timescale on the horizontal axis denotes the time difference between pump and probe beam. For negative times, the probe beam arrives before the pump beam and at $t = 0$, both beams arrive simultaneously.

5.2 Results and Discussion

A selection of time domain data for different field values and corresponding fits using equation 17 are shown in figures 5.2 to 5.7. For low field values, the overlap peak is clearly separated from the first oscillation (fig. 5.3). However, for higher field values the left flank of the first oscillation becomes distorted and tends to merge with the overlap peak (fig. 5.6 and 5.7). This distorted area can not be described by equation 17 and must be excluded from the fit. Note that the typical timescale of damping, τ , is independent of the oscillation frequency. This means that the number of oscillations observed increases with increasing frequency, or equivalent, the damping per oscillation decreases with increasing frequency. The damping is discussed in chapter 6.

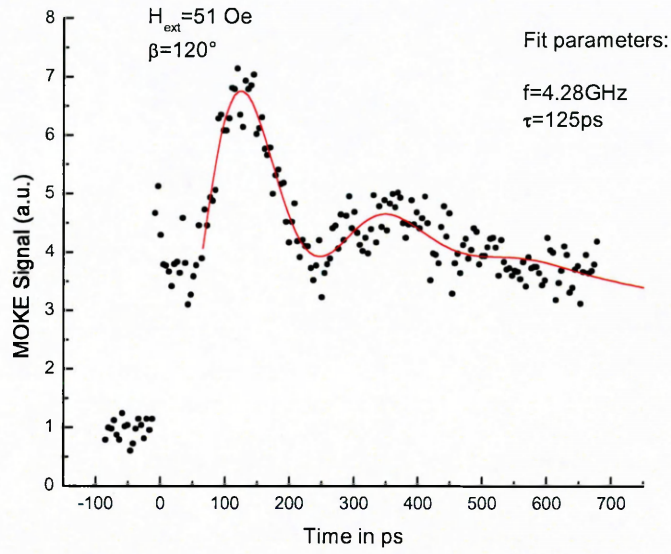


Figure 5.2: Magnetization oscillations measured with TR-MOKE. The external field of 51Oe is oriented along the hard axis ($\beta = 120^\circ$). The timescale on the horizontal axis denotes the time difference between pump and probe beam. The red curve is a fit using equation 17.

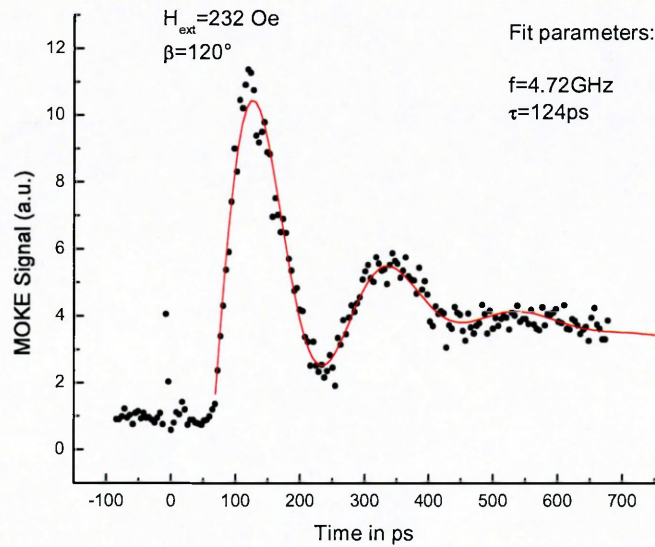


Figure 5.3: Magnetization oscillations measured with TR-MOKE. The external field of 232Oe is oriented along the hard axis ($\beta = 120^\circ$). The timescale on the horizontal axis denotes the time difference between pump and probe beam. The red curve is a fit using equation 17.

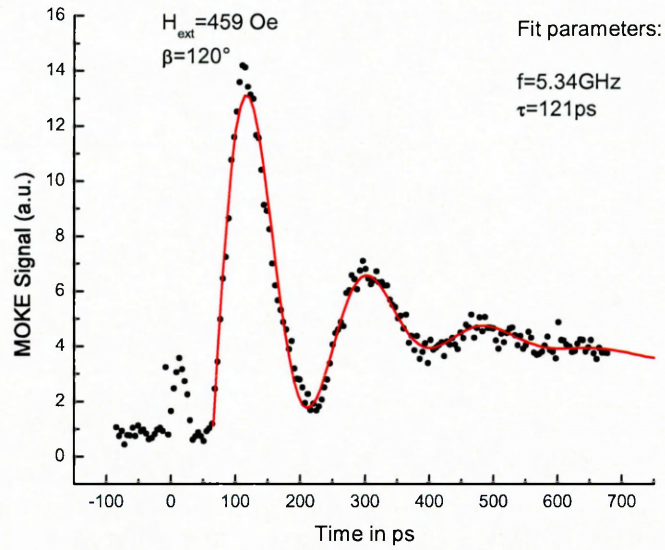


Figure 5.4: Magnetization oscillations measured with TR-MOKE. The external field of 459Oe is oriented along the hard axis ($\beta = 120^\circ$). The timescale on the horizontal axis denotes the time difference between pump and probe beam. The red curve is a fit using equation 17.

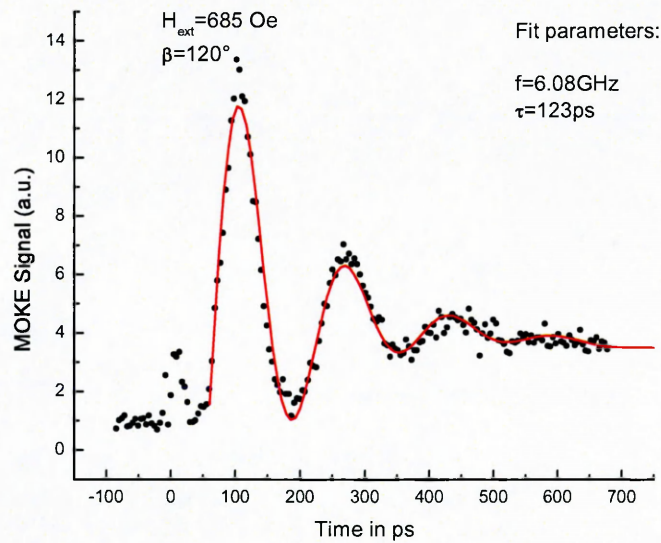


Figure 5.5: Magnetization oscillations measured with TR-MOKE. The external field of 685Oe is oriented along the hard axis ($\beta = 120^\circ$). The timescale on the horizontal axis denotes the time difference between pump and probe beam. The red curve is a fit using equation 17.

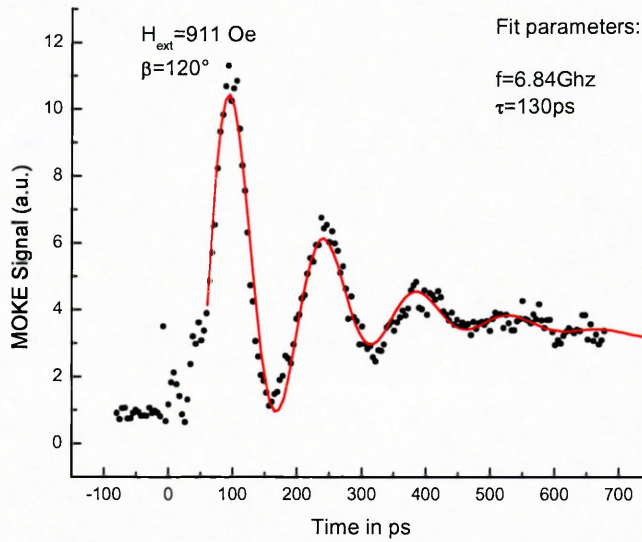


Figure 5.6: Magnetization oscillations measured with TR-MOKE. The external field of 911Oe is oriented along the hard axis ($\beta = 120^\circ$). The timescale on the horizontal axis denotes the time difference between pump and probe beam. The red curve is a fit using equation 17.

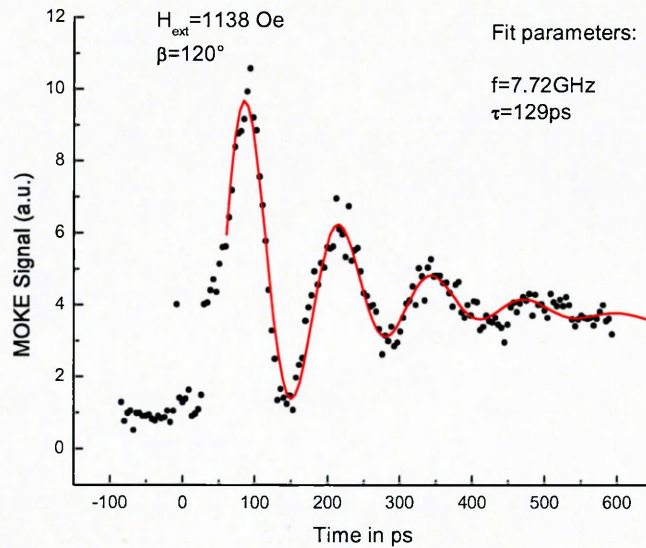


Figure 5.7: Magnetization oscillations measured with TR-MOKE. The external field of 1138Oe is oriented along the hard axis ($\beta = 120^\circ$). The timescale on the horizontal axis denotes the time difference between pump and probe beam. The red curve is a fit using equation 17.

The magnetization dynamics are measured as a function of the external field for two different field angles β . The first angle, $\beta = 120^\circ$, corresponds to a hard axis (fig. 5.8) and the second angle, $\beta = 20^\circ$ is close to an easy-easy axis (fig. 5.9). A measurement for $\beta = 0^\circ$ (easy-easy axis) is not presented, since it was impossible to excite oscillations for that field direction over a wide range of field values. It is difficult to excite oscillations on an easy axis because the laser excitation mainly reduces the magnitude of the anisotropy field but it is not changing its direction. Only for higher fields an excitation is possible, since small out of plane field components (the field is never exactly in the plane of the sample) in combination with the effective demagnetization field (which is altered by the laser) can also cause precession motion [23]. Additionally, the frequency is measured as a function of β at constant field values of 459 Oe and 685 Oe (fig. 5.10 and 5.11 respectively).

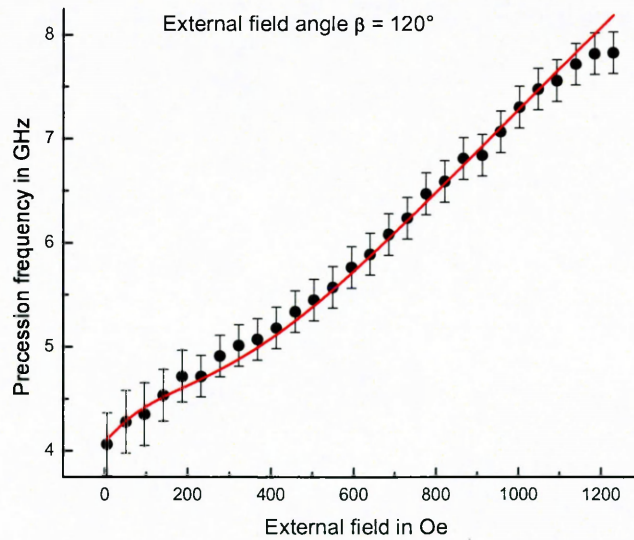


Figure 5.8: Precession frequency as a function of the external field measured for an external field angle $\beta = 120^\circ$. The red line represents the fit using equation 23 with the parameters given in table 5.1.

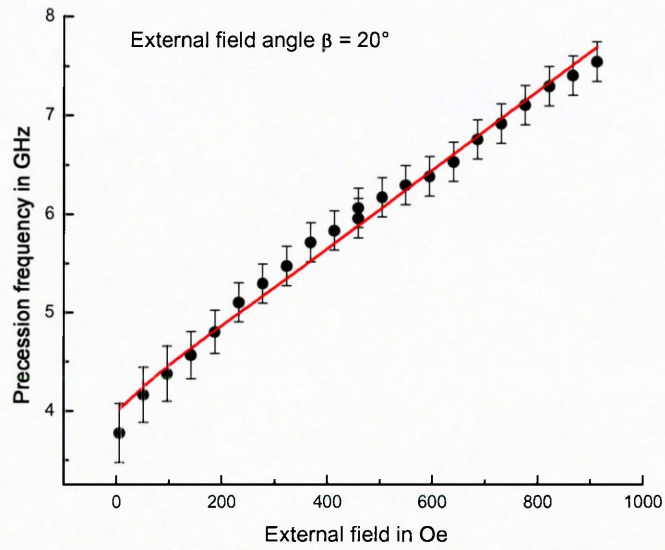


Figure 5.9: Precession frequency as a function of the external field measured for an external field angle $\beta = 20^\circ$. The red line represents the fit using equation 23 with the parameters given in table 5.1.

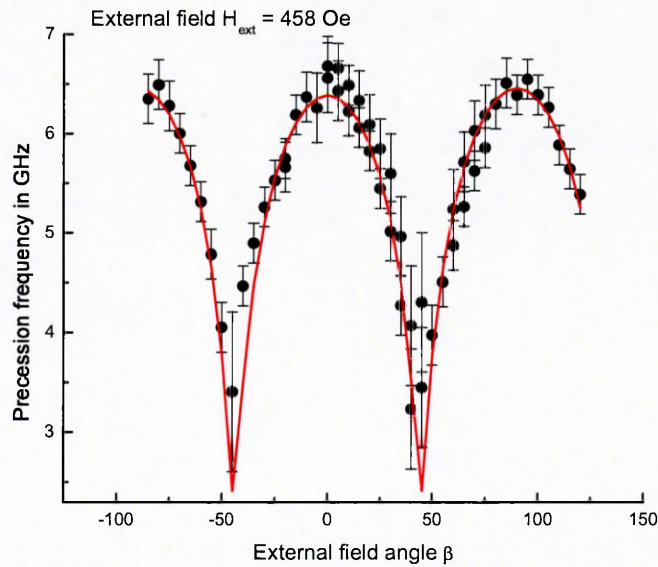


Figure 5.10: Precession frequency as a function of the external field angle β measured for an external field value $H_{ext} = 458 \text{ Oe}$. The red line represents the fit using equation 23 with the parameters given in table 5.1.

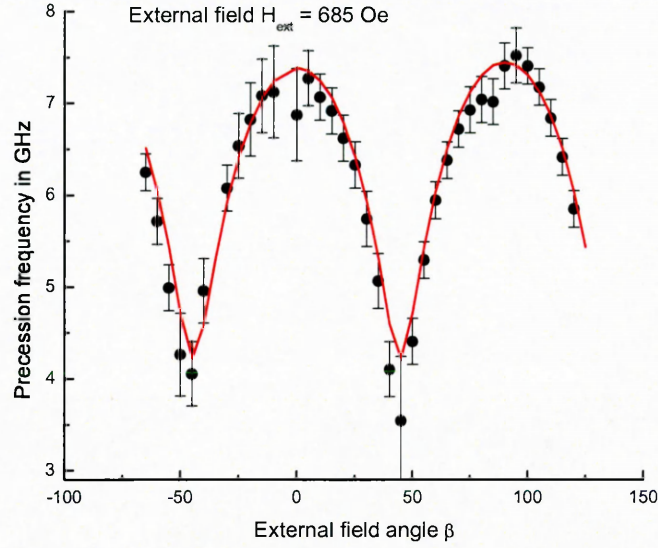


Figure 5.11: Precession frequency as a function of the external field angle β measured for an external field value $H_{ext} = 685 \text{ Oe}$. The red line represents the fit using equation 23 with the parameters given in table 5.1.

Both, field and angle dependent data are fitted with equation 23, which depends on derivatives of the free energy F evaluated at the equilibrium position of magnetization (ϕ_0, θ_0) . The free energy is given by

$$F = E_{ext} + E_{demag} + E_{anisotropy} \quad (28)$$

where $E_{ext} = \vec{H}_{ext} \cdot \vec{M}$ and $E_{demag} = 2\pi M_S^2 \cos \theta$ are the energies due to the interaction of the magnetization with the external field and demagnetization field, respectively. The anisotropy energy $E_{anisotropy} = E_{cubic} + E_{tetragonal} + E_{uniaxial}$ is assumed to be the sum of a cubic, a tetragonal and a uniaxial term as described in the sample section. The equilibrium direction of magnetization (ϕ_0, θ_0) is determined by the conditions $\frac{\partial F}{\partial \theta} \equiv 0$

and $\frac{\partial F}{\partial \phi} \equiv 0$. These two equations can only be solved numerically which means that the data fitting also has to be done numerically.

The fitting procedure minimizes the least squares error (LSE) through an iterative method: first the LSE is calculated for an initial set of parameters. In the next step, the algorithm varies the parameters by a small amount and calculates the LSE for all possible combinations of those varied parameters. The parameter set with the smallest LSE is used to replace the initial set. This process is repeated until a minimum is obtained. In order to avoid local minima, the starting parameters are chosen randomly within a user defined range. A drawback of this method is the fact that the runtime of the program scales exponentially with the number of free parameters. On a 1.8Ghz Centrino notebook, the Mathematica program used in this thesis is able to handle 4 free parameters in a reasonable time. In this thesis, 3 free parameters were determined by fitting. The best results are obtained by fitting the four datasets (fig. 5.8 – 5.11) simultaneously, meaning that the sum of the four LSEs is minimized.

The fits reproduce the measured data well for all four datasets. During fitting, saturation magnetization, cubic anisotropy constant and the g-factor are fixed to the values reported for bulk Ni. This is reasonable, since the sample is a relatively thick film (30 nm), containing about 170 monolayers of Ni. Three parameters are determined by the fitting process: the uniaxial anisotropy constant, U_1 , and the tetragonal in and out of plane anisotropy constants, T_1 and T_{perp} respectively. Both anisotropies, tetragonal and uniaxial, are most likely caused by the distorted NiO layer which grows during in situ annealing. U_1 , T_1 and T_{perp} therefore can be regarded as changes of the anisotropy caused

by the lattice distortions mentioned in chapter 3. While the uniaxial anisotropy is clearly visible in the in-plane static MOKE measurements discussed in chapter 4, the tetragonal component remains hidden. For the (001) plane, the tetragonal in plane component has the same functional dependence as the cubic anisotropy and therefore does not change the four fold symmetry of the coercivity. The tetragonal out of plane component can not be detected by in plane MOKE. Table 5.1 gives an overview on the parameters of equation 23.

Parameter	Value	Error	Reference
g-factor	2.21	not specified by source	Fixed to the value for bulk Nickel given by [10]
M_s (Saturation magnetization)	484.1 emu/cm^3	not specified by source	Fixed to the value for bulk Nickel given by [11]
K1 (First cubic anisotropy constant for Ni)	-57000 erg/cm^3	not specified by source	Fixed to the value for bulk Nickel given by [10]
U1 (Uniaxial anisotropy constant)	-2008 erg/cm^3	20%	Free parameter – value determined by this work
T1 (Tetragonal in plane anisotropy constant)	-27554 erg/cm^3	10%	Free parameter – value determined by this work
T_{perp} (Tetragonal out of plane anisotropy constant)	-292072 erg/cm^3	10%	Free parameter – value determined by this work

Table 5.1: Overview on the parameters of equation 23.

Assuming the coherent rotation model [24], where the magnetization of a sample always follows the energy gradient, one would expect the following equation to be fulfilled:

$$\frac{H_C(\text{easy} - \text{hard axis})}{H_C(\text{easy} - \text{easy axis})} \approx \frac{E_{\text{anisotropy}}(\text{easy} - \text{hard axis})}{E_{\text{anisotropy}}(\text{easy} - \text{easy axis})} \quad (28)$$

This essentially means that the field necessary to switch the magnetization, is proportional to the anisotropy energy that it has to overcome.

The right side of equation 28 is given by $\frac{\left(\frac{KI}{4} + \frac{TI}{4}\right) - UI}{\frac{KI}{4} + \frac{TI}{4}} = 1 - \frac{UI}{\frac{KI}{4} + \frac{TI}{4}} \approx 90.5\%$ and the

left side evaluates to $\frac{94 \text{ Oe}}{103 \text{ Oe}} \approx 91.3\%$. The factor $\frac{1}{4}$ comes from the anisotropy energy

(eq. 25 and 27). This estimate shows that the anisotropy constants obtained with TR-MOKE agree with the coercivity values from the S-MOKE measurements presented in chapter 4.

The tetragonal in plane anisotropy, $T1$, enhances the cubic energy by $\frac{TI}{KI} \approx 48\%$, compared to bulk nickel. At the same time, the tetragonal out of plane component reduces the effective demagnetization field by $\frac{T_{\text{perp}}}{E_{\text{Demag}}} \approx -20\%$. However, the effective demagnetization field still restricts the magnetization to the plane of the sample, since it is fifty times larger than the in plane anisotropy fields.

Summarizing, the precession frequency of the magnetization is determined by an all optical pump probe technique. Field and angular dependence of the precession are studied and the magneto-crystalline anisotropy constants are determined by fitting the

data to the Smit – Suhl formula (Eq. 23). The anisotropy constants agree with the static MOKE measurements described in chapter 4 and they show that the interfacial NiO layer is responsible for a 48% enhancement of the cubic anisotropy as well as a 20% decrease in the effective demagnetization field.

6 Damping

The dimensionless Gilbert damping parameter, α , is extracted from the field and angular dependent TR-MOKE measurements. α is calculated from the TR-MOKE fitting parameter, τ , using the relation $\alpha = \frac{1}{\omega\tau}$. The results are shown in figures 6.1 – 6.4. The

red curves in these figures are explained later in this chapter.

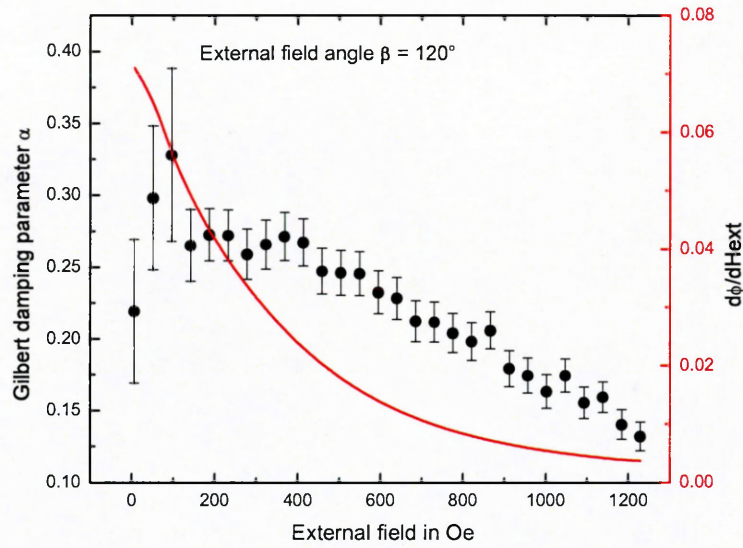


Figure 6.1: Gilbert damping as a function of the external field. The field is oriented along the hard axis ($\beta = 120^\circ$). The red curve represents the derivative of the magnetization's equilibrium angle with respect to H_{ext} .

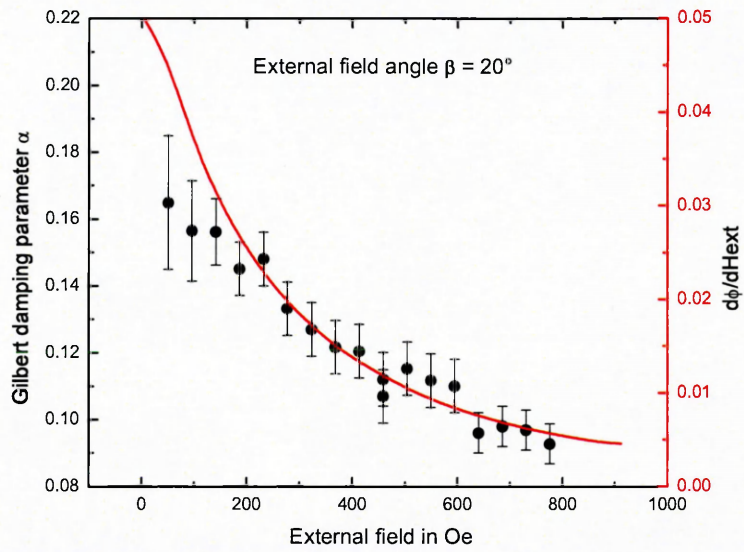


Figure 6.2: Gilbert damping as a function of the external field. The field angle is $\beta = 20^\circ$. The red curve represents the derivative of the magnetization's equilibrium angle with respect to H_{ext} .

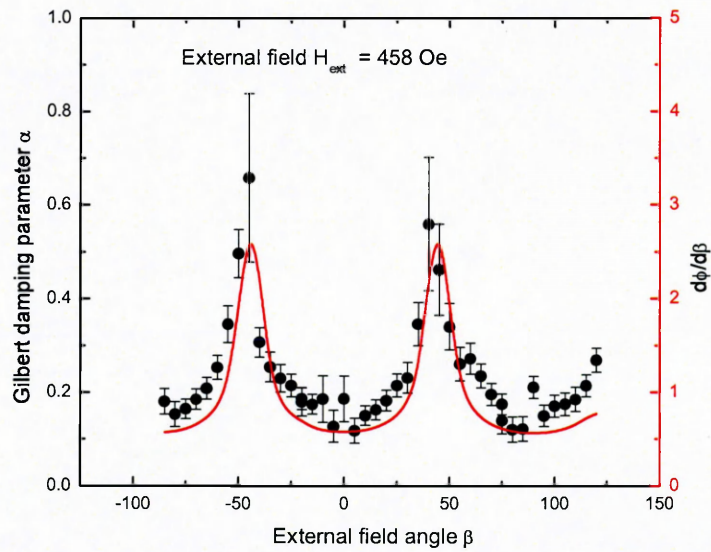


Figure 6.3: Gilbert damping as a function of the external field angle β with $H_{ext} = 458 \text{ Oe}$. The red curve represents the derivative of the magnetization's equilibrium angle with respect to β .

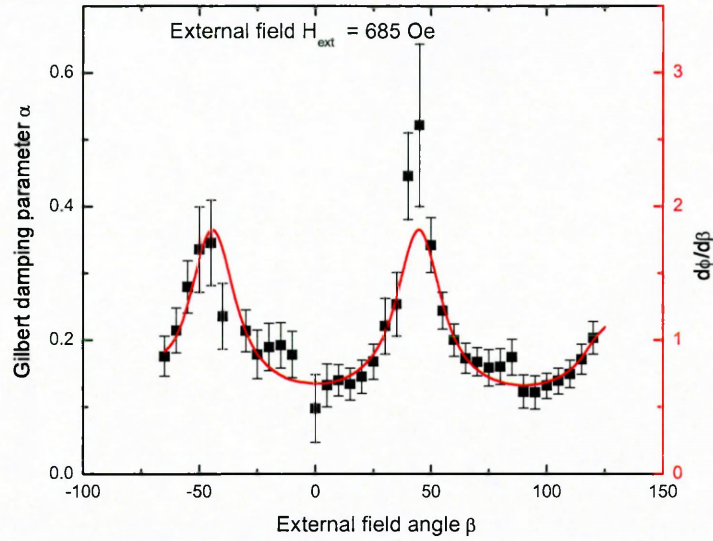


Figure 6.4: Gilbert damping as a function of the external field angle β with $H_{\text{ext}} = 685 \text{ Oe}$. The red curve represents the derivative of the magnetization's equilibrium angle with respect to β .

α takes values between 0.09 and 0.3 for the field dependent measurements and lies between 0.1 and 0.6 for the angle dependent measurements. This is higher than $\alpha = 0.05$ reported by van Kampen et. al. for a single layer nickel film [5]. However, Djordjevic et. al. [17] reported much higher values up to $\alpha = 0.8$ for Ni Cr bilayers. Others reported values of $\alpha \approx 0.3$ for other ferromagnetic materials [9, 16].

Both, field and angle dependent data, show a relation between damping and precession frequency: α decreases for increasing frequency. This observation is consistent with what is reported in the literature. The phenomenon is well known and can be observed in both, frequency domain FMR experiments [25, 26] and time domain pump probe experiments [16, 17]. Figures 6.5 and 6.6 show α as a function of the precession frequency for both, field and angle dependent measurements.

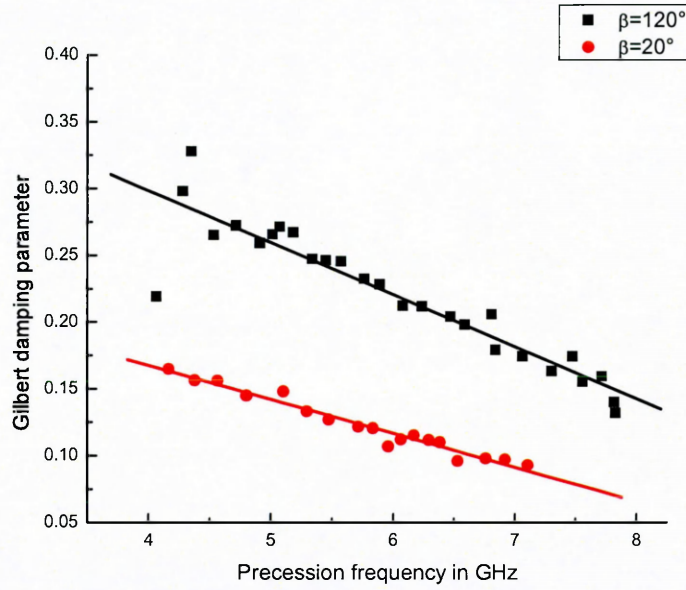


Figure 6.5: Gilbert damping as a function of the precession frequency. The external field angle, β , is fixed to 120° and 20° for the black and red curve, respectively. The frequency is varied by changing the external field H_{ext} . The two lines are linear fits to the data.

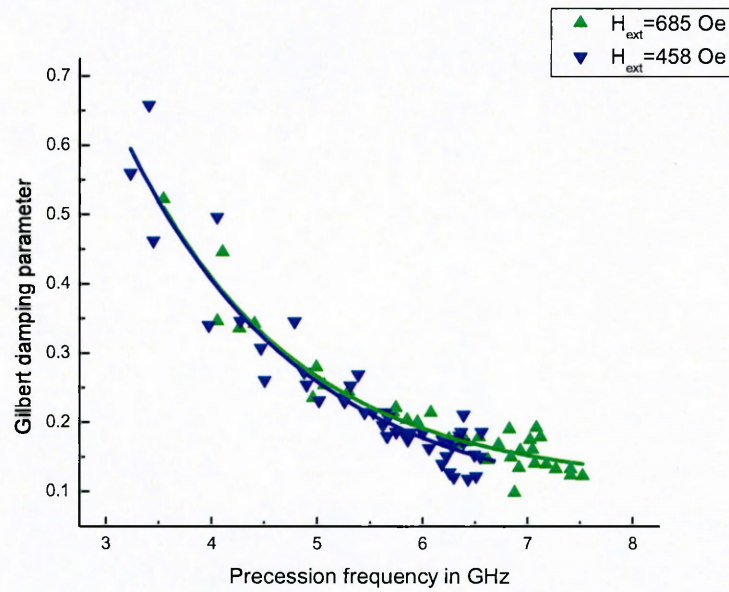


Figure 6.6: Gilbert damping as a function of the precession frequency. The external field value, H_{ext} , is fixed to 685Oe and 458Oe for the green and blue curve, respectively. The frequency is varied by changing the external field angle β . The two curves are first order exponential fits to the data.

The frequency dependence of α is linear for the field dependent measurements (fig 6.5) and exponential for the angle dependent measurements (fig. 6.6). The data are fitted with a linear and an exponential term, respectively.

One can see that for the field dependent measurements, shown in figure 6.5, α depends linear on the frequency. In this case y-intercept and slope depend on the orientation of the external field with respect to the sample's anisotropy. If on the other hand, the field angle is changed while applying constant field; the resulting frequency dependence follows an exponential law, as shown in figure 6.6.

This finding shows that the frequency dependence of the Gilbert damping, α , depends on the angle of the external field with respect to the crystallographic orientation of the sample. Furthermore, the angle dependent data in figure 6.6 indicates, that the frequency dependence of α does not depend on the value of the external field. At least not for the range of fields applied in the experiment.

In the current literature, there are reports about changes in the frequency dependence of the damping for different substrates or capping layers [16]. Another recent publication, [17], reported a change in frequency dependence of α for Ni films with different thicknesses. The authors varied the frequency by changing the magnitude of the external field and found that the frequency dependence of α , strongly depends on the thickness of the sample as shown in figure 6.7.

The findings of this thesis show that the frequency dependence of the Gilbert damping is not only affected by the sample parameters. It also strongly depends on the relative orientation of the external field with respect to the sample's anisotropy.

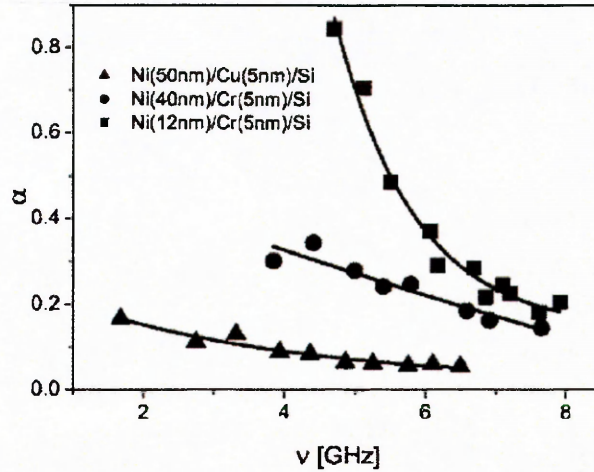


Figure 6.7: Gilbert damping parameter as a function of the frequency for three different Ni samples. The frequency is varied by a variation of the applied field. Figure taken from ref. [17]

Aside from the fact that the frequency dependence of the damping depends on the crystallographic orientation of the sample, the data presented in this thesis agrees with previous findings. The damping is commonly attributed to two-magnon scattering processes [16, 27, 28], where the coherent precession mode ($k=0$) decays into degenerated modes with $k>0$. This process is not momentum conserving and therefore requires defects to absorb the momentum [29, 30]. Beside normal lattice defects, a ferromagnet – antiferromagnet interface, like the Ni-NiO interface, can be responsible for two-magnon scattering [16]. The two magnon scattering is likely to occur in our sample because of the lattice defects at the NiO interface. An example for a frequency dependent damping, similar to the one displayed in figures 6.5 and 6.6, is shown in figure 6.7.

A second mechanism for magnetization damping is the local resonance model, which assumes, that the magnetization in adjacent magnetic domains precesses with slightly different frequencies [31]. Over time, the magnetization vectors of the different domains dephase and cause an effective damping. From this model, one would expect the

damping to be strong if there are a large number of domains with different resonance frequencies.

In general, the number of domains increases if the magnetization direction is changed because it is energetically more favorable for the material to form smaller domains that can change their magnetic moment independently. Hence, the faster the magnetization is changing, the higher the damping should be. The red curves, shown in figures 6.1 – 6.4, represent the derivatives of magnetization's equilibrium angle with respect to the parameter varied during the measurement. There is a clear trend throughout all four figures, showing that the damping increases as the magnetization angle changes more rapidly. For a fast change in the equilibrium angle of \vec{M} , more domains are forming. Hence the dephasing effect becomes more pronounced and results in a higher damping as can be seen in figures 6.1 – 6.4.

In order to determine which mechanism dominates the damping in this sample, further experiments have to be conducted. The contribution of the two magnon scattering for example can be determined by applying the magnetic field out of the plane of the sample, since that suppresses two magnon scattering. [30].

Summarizing, the Gilbert damping was extracted from time domain pump probe measurements and its field, angle and frequency dependence were studied. The results can be explained equally well by two different models: the two magnon model, which damps through scattering into modes with a higher wave number and the local resonance model, that causes an effective damping through dephasing.

In general the data shows the same trend as the results reported in the literature. However, in contrast to current literature, it is found that the Gilbert damping can not just be regarded as a function of the materials magnetic resonance frequency. It rather seems to depend strongly on the orientation of the external field with respect to magneto-crystalline anisotropy.

7 Conclusions

The magnetization dynamics and anisotropy of a Ni/NiO bilayer have been studied by time-resolved pump-probe MOKE and static MOKE. The data has been analyzed with respect to crystalline anisotropy and intrinsic damping.

Field and angular dependence of the magnetization precession frequency have been measured and are found to be in agreement with the Smit – Suhl formula for FMR precession.

The anisotropy components obtained from the time-resolved MOKE measurement show that the NiO layer causes a 48% increase of the cubic anisotropy compared to pure nickel and lowers the effective demagnetization field by 20%. The value determined for the uniaxial component is consistent with static MOKE measurements.

The Gilbert damping was extracted from time-domain pump-probe MOKE measurements and its field, angle and frequency dependence were studied. The results can be explained equally well by the two-magnon model and the local resonance model. Further experiments are necessary to determine the contribution of the two models to the damping.

The Gilbert damping parameter is found to depend strongly on the orientation of the external field with respect to magneto-crystalline anisotropy.

References

- [1] P. Grünberg, R. Schreiber, Y. Pang, M. B. Brodsky, and H. Sowers, *Phys. Rev. Lett.* **57**, 2442 (1986)
- [2] M. N. Baibich, J. M. Broto, A. Fert, F. Nguyen Van Dau, F. Petroff, P. Eitenne, G. Creuzet, A. Friedrich, and J. Chazelas, *Phys. Rev. Lett.* **61**, 2472 (1988)
- [3] J. Nogués and I. K. Schuller, *J. Magn. Magn. Mater.* **192**, 203 (1999)
- [4] V. Skumryev, S. Stoyanov, Y. Zhang, G. Hadjipanayis, D. Givord, and J. Nogués, *Nature* **423**, 850 (2003)
- [5] M. van Kampen, C. Jozsa, J. T. Kohlhepp, P. LeClair, L. Lagae, W. J. M. de Jonge, and B. Koopmans, *Phys. Rev. Lett.* **88**, 227201 (2002)
- [6] P. S. Pershan, *J. Appl. Phys.* **38**, 1482 (1967)
- [7] Z. Q. Qiu, and S. D. Bader, *Rev. Sci. Instrum.* **71**, 1243 (2000)
- [8] M. Mansuripur, *Classical Optics and its Applications*, Cambridge University Press (2002)
- [9] K. A. Seu, *Ultrafast and Static MOKE Studies of Exchange-Biased Co Systems*, Ph.D. Thesis, College of William & Mary, 2006
- [10] S. Chikazumi, *Physics of Ferromagnetism*, Oxford (1997)
- [11] B. D. Cullity, *Introduction to Magnetic Materials*, Addison-Wesley (1972)
- [12] M. d'Aquino, *Nonlinear Magnetization Dynamics in Thin-Films and Nanoparticles*, Doctorate Thesis in Electrical Engineering, Università Degli Studi di Napoli, 2004
- [13] Jeongwon Ho, F.C. Khanna and B.C. Choi, *PhysRevLett.*92.097601 (2004)
- [14] T. L. Gilbert, *Phys. Rev.* **100**, 1243 (1955)
- [15] T. J. Silva, C. S. Lee, T. M. Crawford, and C. T. Rogers, *J. Appl. Phys.* **85**, 7849 (1999)
- [16] G. Woltersdorf, M. Buess, B. Heinrich, and C. H. Back, *Phys. Rev. Lett.* **95**, 037401 (2005)

- [17] Marija Djordjevic, Gerrit Eilers, Anne Parge, Markus Münzenberg, and J. S. Moodera, *Journal of Applied Physics* 99, 08F308 (2006)
- [18] H. Suhl, *Phys. Rev.* 97, 555 (1955)
- [19] S. V. Vonsovskii, *Ferromagnetic resonance*, Pergamon Press (1966)
- [20] R.A. Lukaszew, M. Mitra, Z. Zhang and M. Yeadon, *The Eur. Phys. J. B* 45 181-184 (2005)
- [21] D. Talbayev, H. Zhao, G. Lüpke, A. Venimadhav and Qi Li, *PhysRev. B* 73, 014417 (2006)
- [22] E. Beaurepaire, J.-C. Merle, A. Daunois, and J.-Y. Bigot, *Phys. Rev. Lett.* 76, 4250 (1996)
- [23] M. van Kampen, B. Koopmans, J.T. Kohlhepp, W.J.M. de Jonge, *Journal of Magnetism and Magnetic Materials* 240 (2002) 291–293
- [24] Stoner E C and Wohlfarth E P, *Phil. Trans. Roy. Soc. A*240:599–642 (1948)
- [25] P. Wolf, *Journal of Applied Physics* 32, 95S (1961)
- [26] R. Urban, G. Woltersdorf, and B. Heinrich, *Physical Review Letters* 87, 217204 (2001)
- [27] B. Heinrich et al., *Phys. Rev. Lett.* 59, 1756 (1987)
- [28] J. Lindner et al., *Phys. Rev. B* 68, 060102 (2003)
- [29] Rodrigo Arias and D. L. Mills, *Phys. Rev. B* 60, 7395 (1999)
- [30] M. J. Hurben and C. E. Patton, *Journal of Applied Physics* 83, 4344 (1998)
- [31] R. D. McMichael and D. J. Twisselmann, Andrew Kunz, *Phys. Rev. Lett.* 90, 227601 (2003)